

Group 6 metal complexes as electrocatalysts of CO₂ reduction: strong substituent control of the reduction path of [Mo(η^3 -allyl)(CO)₂(x,x'-dimethyl-2,2'-bipyridine)(NCS)] (x = 4–6)

Article

Accepted Version

Taylor, J. O., Veenstra, F. L. P., Chippindale, A. M. ORCID: <https://orcid.org/0000-0002-5918-8701>, Calhorda, M. J. and Hartl, F. ORCID: <https://orcid.org/0000-0002-7013-5360> (2019) Group 6 metal complexes as electrocatalysts of CO₂ reduction: strong substituent control of the reduction path of [Mo(η^3 -allyl)(CO)₂(x,x'-dimethyl-2,2'-bipyridine)(NCS)] (x = 4–6). *Organometallics*, 38 (6). pp. 1372-1390. ISSN 1520-6041 doi: <https://doi.org/10.1021/acs.organomet.8b00676> Available at <https://centaur.reading.ac.uk/81186/>

It is advisable to refer to the publisher's version if you intend to cite from the work. See [Guidance on citing](#).

To link to this article DOI: <http://dx.doi.org/10.1021/acs.organomet.8b00676>

Publisher: American Chemical Society

including copyright law. Copyright and IPR is retained by the creators or other copyright holders. Terms and conditions for use of this material are defined in the [End User Agreement](#).

www.reading.ac.uk/centaur

CentAUR

Central Archive at the University of Reading

Reading's research outputs online

Group-6 Complexes as Electrocatalysts of CO₂ Reduction: Strong Substituent Control of the Reduction Path of [Mo(η^3 -allyl)(CO)₂(*x,x'*-dimethyl-2,2'-bipyridine)(NCS)] (*x* = 4-6)

James O. Taylor,¹ Florentine L. P. Veenstra,^{1,2} Ann M. Chippindale,¹ Maria José Calhorda,³ František Hartl^{1,*}

¹Department of Chemistry, University of Reading, Reading, RG6 6AD, United Kingdom.

²Institute for Chemical and Bioengineering, Department of Chemistry and Applied Biosciences, ETH Hönggerberg, Vladimir-Prelog-Weg 1, 8093 Zurich, Switzerland

³Centro de Química e Bioquímica and BioISI - Biosystems & Integrative Sciences Institute, Departamento de Química e Bioquímica, Faculdade de Ciências, Universidade de Lisboa, 1749-016 Lisboa, Portugal

ABSTRACT: A series of complexes [Mo(η^3 -allyl)(CO)₂(*x,x'*-dmbipy)(NCS)] (dmbipy = dimethyl-2,2'-bipyridine; *x* = 4-6) have been synthesized and their electrochemical reduction investigated using combined cyclic voltammetry (CV) and variable-temperature spectroelectrochemistry (IR/UV-vis SEC) in tetrahydrofuran (THF) and butyronitrile (PrCN), at gold and platinum electrodes. The experimental results, strongly supported by DFT calculations, indicate that the general cathodic path of these Group-6 organometallic complexes is closely related to that of the intensively studied class of Mn tricarbonyl α -diimine complexes, themselves recently identified as important smart materials for catalytic CO₂ reduction. The dimethyl substitution on the 2,2'-bipyridine ligand backbone has presented new insights into this emerging class of catalysts. For the first time, the 2e⁻ reduced 5-coordinate anions [Mo(η^3 -allyl)(CO)₂(*x,x'*-dmbipy)]⁻ were directly observed with IR SEC. The role of steric and electronic effects in determining the reduction-induced reactivity was also investigated. For the 6,6'-dmbipy, the primary 1e⁻ reduced radical anions exert unusual stability radically changing the follow up cathodic path. The 5-coordinate anion [Mo(η^3 -allyl)(CO)₂(6,6'-dmbipy)]⁻ remains stable at low temperature in strongly coordinating butyronitrile and does not undergo dimerization at elevated temperature, in sharp contrast to reactive [Mo(η^3 -allyl)(CO)₂(4,4'-dmbipy)]⁻ that tends to dimerize in a reaction with the parent complex. The complex with the 5,5'-dmbipy ligand combines both types of reactivity. Under aprotic conditions, the different properties of [Mo(η^3 -allyl)(CO)₂(*x,x'*-dmbipy)]⁻ are also reflected in their reactivity towards CO₂. Preliminary CV and IR SEC results reveal differences in the strength of CO₂ coordination at the free axial position. Catalytic waves attributed to the generation of the 5-coordinate anions were observed by CV, but only a modest catalytic performance towards the production of formate was demonstrated by IR SEC. For 6,6'-dmbipy, a stronger catalytic effect was observed for the Au cathode compared to Pt.

INTRODUCTION

Atmospheric levels of anthropogenic CO₂ have continued to increase unabated for several years, driving a concurrent rise in yearly average temperatures and extreme weather patterns.¹ Although it has an obvious damaging impact on the environment, CO₂ itself has potential to become a sustainable source of carbon-based fuels and chemical feedstocks for Fischer-Tropsch chemistry. To fulfill this potential, CO₂ must

first be reduced electro- or photochemically, converting it from a harmful by-product of industry to compounds with the aforementioned applications.^{2,3} However, the direct electrochemical reduction to CO₂⁻ is hindered by large overpotentials and one must take advantage of proton-coupled reduction pathways.^{3,4} An exception is a dinuclear Cu(I) catalyst reported recently by Bowman and co-workers, which reduces CO₂ from the air to ox-

alate isolated as a lithium salt.⁵ In comparison, the proton-coupled paths have significantly reduced energy barriers to catalysis but they must be promoted by homogenous or heterogenous (Cu) transition-metal catalysts. The effect of the catalyst is two-fold, enabling reduction of CO₂ at much lower overpotentials whilst also allowing one to handle a larger number of proton- and electron-transfer steps facilitating the transformation to more complex and valuable reduction products such as formaldehyde, methanol or methane.⁶ Of the many homogeneous transition-metal electrocatalysts of CO₂ reduction known in the literature, the most widely studied have been those based on the noble metals, Re^{7–12}, Ru^{10,13–15}, Rh¹⁶ and Ir.^{17,18} Although first reported almost 40 years ago, they are still offering up both interesting redox properties and synthetic challenges. The high costs of these metals, as well as a strong competition for the limited supply from the electronics industry, largely preclude the possibility of any industrial-scale system. Thus, efforts now focus on the more abundant metals, Mn, Fe, Co¹⁹, and Ni^{20,21}. Highly promising are the systems of [Mn(CO)₃(α -diimine)X] (X = (pseudo)halide), only recently found to be catalytically active at potentials similar to the analogous complexes of rhenium, in the presence of Brønsted or Lewis acids.^{22–28} The Fe-porphyrin systems are also highly efficient catalysts of CO₂ reduction, but synthetically challenging to prepare.^{29–31}

Surprisingly, and despite the analogues found in Nature, the Group-6 metal triad (Cr, Mo, W) has largely been ignored by the wider community. This has been highlighted in several recent comprehensive reviews of the field.^{32–34} Preliminary studies of Group-6 complexes show a potential to catalytically reduce CO₂ with a comparable activity and efficiency to that of the widely studied Group-7 systems. Recently, it was reported that Group-6 hexacarbonyl complexes can behave catalytically toward CO₂.³⁵ This is highly unusual, as most catalysts reported to date bear a redox-active ligand acting as both an electron reservoir and a parking place for the protons required for catalysis. The hexacarbonyl is reduced by 2e⁻ to form [M(CO)₅]²⁻ that can bind CO₂ and transform to [M(CO)₅(CO₂)]²⁻; under anhydrous conditions, the major product of the reduction is CO. Interestingly, addition of water or another proton source inhibits the activity of the catalyst, most likely due to competing formation of H₂ from [M(CO)₅H]⁻. A comparison with [M(CO)₅]⁻ (M = Re or Mn), formed by the reduction of the corresponding decacarbonyl dimers, shows that the Group-7 metals are not active toward CO₂ in this manner. Instead, they simply bind CO₂ and require a non-innocent ligand to trigger the reduction. The difference in their reactivity may simply be explained by the fact that the Group-6 [M(CO)₅]²⁻ species are better reducing agents, due to the negative charge experiencing less nuclear charge than the comparable Group-7 species. Apart from this, the limited literature regarding Group-6 catalysts has mostly focused on the family of [M(CO)₄(α -diimine)] catalysts.^{36–40} The first of these studied as a catalyst of CO₂ reduction was [Mo(CO)₄(bipy)] (bipy = 2,2'-bipyridine).^{36,37} The parent complex is reduced in two consecutive 1e⁻ steps to form first the corresponding radical anion and then the catalytically active 5-coordinate species, [Mo(CO)₃(bipy)]²⁻. The latter is iso-electronic with the Group-7 catalysts, [M(CO)₃(bipy)]⁻ (M = Re, Mn), formed by 2e⁻ (ECE) reduction of [M(CO)₃(bipy)X] (X = (pseudo)halide).

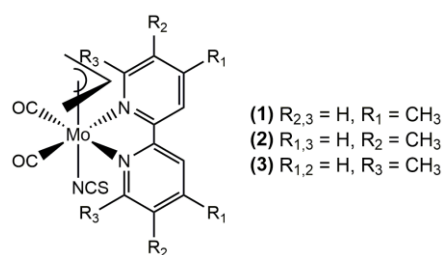
Unlike their Group-7 cousins, [Mo(CO)₄(α -diimine)] (α -diimine = 2,2'-bipyridine (bipy) and *x,x'*-dimethyl-bipyridine

(dmbipy, *x* = 4-6) show higher sensitivity to the cathodic material.³⁷ This can be exploited in the form of a low-energy pathway only accessible with the use of a gold cathode that facilitates CO dissociation from the usually stable radical anion, [Mo(CO)₄(bipy)]⁻, converting it to [Mo(CO)₃(bipy)]⁻. The latter 5-coordinate complex is reducible to the dianionic catalyst at a cathodic potential only slightly more negative than the initial reduction of the neutral tetracarbonyl parent, thereby bypassing the energetically demanding formation of the unstable dianion, [Mo(CO)₄(bipy)]²⁻. This CO dissociation-first pathway is similar to the low-energy protonation-first pathway reported for [Mn(CO)₃(bipy)Br].⁴¹ These observations have been confirmed by Cowan and co-workers using sum frequency generation (SFG) spectroscopy.⁴² One can also alter the pathway these Group-6 tetracarbonyl catalysts follow, by substitution on the 2,2'-bipyridine rings.³⁹ Advantageous positioning of steric bulk at the 6,6'-position can enhance the CO dissociation from the primary radical anion, improving the catalytic activity, while substitution at the 4,4'-position suppresses the CO dissociation, forcing the catalyst to follow the higher-energy reduction-first pathway. Smart choice of the solvent and electrolyte, especially turning to *N*-methyl-pyrrolidone (NMP), can improve the catalytic efficiency remarkably. Nervi and co-workers³⁸ have described a comparable catalytic action for [M(CO)₄(α -diimine)] (M = Mo, W; α -diimine = 4,6-diphenylbipy, 4-dimethoxyphenyl-6-phenyl-bipy). A higher catalytic activity towards conversion of CO₂ to CO and a unique activation pathway have also been reported for the complexes [M(CO)₄(2,2'-dipyridylamine)] (M = Mo and W), in which the catalytic center resides at the bidentate ligand rather than at the metal.³⁸ The unusual cathodic behaviour of [W(CO)₄(dpa)] has been rationalized with the help of quantum mechanical calculations. The 1e⁻ reduction of the parent complex induces a rearrangement of the dpa ligand with one of the pyridine rings rotating away from the metal centre, which facilitates the reduction of CO₂.⁴³

Inspired by the promising performance of the Group-6 tetracarbonyl catalysts, the related complex [Mo(η^3 -allyl)(CO)₂(bipy)X] (X = (pseudo)halide) was identified as a precursor to the catalytically-active 5-coordinate anion, [Mo(η^3 -allyl)(CO)₂(bipy)]⁻.^{44,45} In an analogous fashion to the well-studied catalyst precursor [Mn(CO)₃(bipy)Br], the radical anion [Mo(η^3 -allyl)(CO)₂(bipy)(NCS)]⁻, formed by the initial one-electron reduction (*E*_{pc} = -1.99 V vs Fc/Fc⁺) is very unstable at room temperature. The concomitant dissociation of the NCS⁻ ligand yields the 5-coordinate radical [Mo(η^3 -allyl)(CO)₂(bipy)][•] that can be reduced at the applied electrode potential of the parent complex to [Mo(η^3 -allyl)(CO)₂(bipy)]⁻. This anion reacts with as yet non-reduced parent, forming the dimer [Mo(η^3 -allyl)(CO)₂(bipy)]₂, the final step of the ECEC pathway. Here the similarity with the Mn-catalysts appears to end. In the original paper⁴⁵ it was claimed that the 5-coordinate anion had been detected by IR spectroelectrochemistry; however, this assignment was only tentative. The main issue to be clarified in this work is under exactly what conditions an IR-detectable quantity of the 5-coordinate anionic catalyst can be formed. Indeed, the dimer-like species produced in this instance appear to be more reactive than the related hexacarbonyl Mn–Mn bound dimers and can only be detected on the relatively short time scale of cyclic voltammetry. The subsequent reduction of the Mo–Mo dimer in the presence of CO₂ is then associated with catalytic current, and infrared monitoring at the catalytic wave reveals the formation of CO and free formate.

Hereinafter, the study of the original (η^3 -allyl)Mo–bipy complex is extended to the series of three x,x' -dmbipy derivatives (Chart 1), with the following goals: (i) to identify (by IR spectroelectrochemistry) the 5-coordinate anions $[\text{Mo}(\eta^3\text{-allyl})(\text{CO})_2(x,x'\text{-dmbipy})]^-$, the proposed active catalysts in these systems, which were misassigned for the reference bipy complex; (ii) to assess the catalytic performance of the 5-coordinate anions via CV and IR SEC; (iii) to investigate the steric and electronic consequences of the dimethyl substitution at the $x = x' = 4, 5$ and 6 positions of the 2,2'-bipyridine ligand on the cathodic paths; (iv) to probe the variation of the cathodic material, Pt and Au, and its impact on the reduction potentials, cathodic pathways and catalytic performance, in analogy with $[\text{Mo}(\text{CO})_{4-n}(x,x'\text{-dmbipy})]^-$ ($n = 0, 1; x = 4-6$).

Chart 1. General molecular structure of the studied complexes $[\text{Mo}(\eta^3\text{-allyl})(\text{CO})_2(x,x'\text{-dmbipy})(\text{NCS})]$ 1 ($x = 4$), 2 ($x = 5$) and 3 ($x = 6$).



EXPERIMENTAL SECTION

Materials and Methods. All syntheses and electrochemical measurements were conducted under a strictly inert atmosphere of dry argon, using standard Schlenk techniques. Solvents were freshly distilled under N_2 from a mixture of Na/benzophenone (tetrahydrofuran, THF), P_2O_5 (acetonitrile, MeCN) or CaH₂ (butyronitrile, PrCN, and dichloromethane, DCM). The electrolyte, tetrabutylammonium hexafluorophosphate (TBAH, Agro-Organics), was recrystallized twice from hot ethanol and dried under vacuum at 80 °C. All other reagents were purchased from Sigma-Aldrich and used as received. The precursor $[\text{Mo}(\eta^3\text{-allyl})(\text{CO})_2(\text{MeCN})_2(\text{NCS})]$ was prepared according to the literature procedure.⁴⁶ All the $[\text{Mo}(\eta^3\text{-allyl})(\text{CO})_2(x,x'\text{-dmbipy})(\text{NCS})]$ complexes were prepared by facile thermal substitution of the labile acetonitrile ligands in $[\text{Mo}(\eta^3\text{-allyl})(\text{CO})_2(\text{MeCN})_2(\text{NCS})]$. For the electrocatalytic studies, solvents were saturated with CO_2 (BOC, < 99.99%) at an atmospheric pressure by short bubbling on a frit.

General Synthesis of $[\text{Mo}(\eta^3\text{-allyl})(\text{CO})_2(x,x'\text{-dmbipy})(\text{NCS})]$. Under argon, a three-necked round-bottom flask was charged with $[\text{Mo}(\eta^3\text{-allyl})(\text{CO})_2(\text{MeCN})_2(\text{NCS})]$ (230 mg, 0.69 mmol) and the appropriate x,x' -dimethyl-2,2'-bipyridine ligand ($x = 4-6$) in a small excess (typically 0.78 mmol). After the addition of dry deaerated DCM (10 mL), the mixture was refluxed at 50 °C for 2 h. The solution was then allowed to cool to ambient temperature and its volume was reduced by half. The remaining solution was transferred to a Schlenk vessel, followed by addition of hexane (5 x 10 mL) to precipitate the crude product that was further purified by extraction with hexane and column chromatography on silica, using dichloromethane:hexane 10:1 (v/v) as eluent. The yields of a red microcrystalline powder varied between 35–55%. X-ray quality crystals were grown by vapour diffusion in hexane/DCM.

$[\text{Mo}(\eta^3\text{-allyl})(\text{CO})_2(4,4'\text{-dmbipy})(\text{NCS})]$ (1). The precursor complex $[\text{Mo}(\eta^3\text{-allyl})(\text{CO})_2(\text{MeCN})_2(\text{NCS})]$ (230 mg, 0.69 mmol) and

4,4'-dmbipy (151 mg, 0.82 mmol) reacted to afford **1** (168 mg, 55 %). ¹H NMR (400 MHz, CD_2Cl_2): δ 8.55 (2H, d, $J = 6$ Hz), 7.85 (2H, s), 7.27 (2H, d, $J = 5.6$ Hz), 3.08 (2H, d, $J = 6.4$ Hz), 2.93 (1H, m), 2.54 (6H, s), 1.34 (2H, d, $J = 6$ Hz); (400 MHz, $(\text{CD}_3)_2\text{SO}$) 8.67 (2H, d, $J = 5.2$ Hz), 8.48 (2H, s), 7.53 (2H, d, $J = 5.6$ Hz), 3.26 (2H, d, $J = 6.8$ Hz), 3.19 (1H, m), 2.52 (6H, s), 1.42 (2H, d, $J = 9.2$ Hz). IR (THF): $\nu(\text{CO})$ 1949, 1869 cm^{-1} , $\nu(\text{CN})$ of NCS^- 2076 cm^{-1} .

$[\text{Mo}(\eta^3\text{-allyl})(\text{CO})_2(5,5'\text{-dmbipy})(\text{NCS})]$ (2). The precursor complex $[\text{Mo}(\eta^3\text{-allyl})(\text{CO})_2(\text{MeCN})_2(\text{NCS})]$ (220 mg, 0.66 mmol) and 5,5'-dmbipy (150 mg, 0.82 mmol) reacted to afford **2** (132 mg, 43 %). ¹H NMR (400 MHz, CD_2Cl_2): δ 8.52 (2H, s), 7.87 (2H, d, $J = 8$ Hz), 7.75 (2H, d, $J = 8$ Hz), 3.12 (2H, d, $J = 8$ Hz), 2.96 (1H, m), 2.40 (6H, s), 1.36 (2H, d, $J = 8$ Hz); (400 MHz, $(\text{CD}_3)_2\text{SO}$) δ 8.64 (2H, s), 8.42 (2H, d, $J = 10$ Hz), 8.05 (2H, d, $J = 10$ Hz), 3.40 (2H, d, $J = 8$ Hz), 3.19 (1H, m), 2.48 (6H, s), 1.40 (2H, d, $J = 8$ Hz). IR (THF): $\nu(\text{CO})$ 1951, 1871 cm^{-1} , $\nu(\text{CN})$ of NCS^- 2076 cm^{-1} .

$[\text{Mo}(\eta^3\text{-allyl})(\text{CO})_2(6,6'\text{-dmbipy})(\text{NCS})]$ (3). The precursor $[\text{Mo}(\eta^3\text{-allyl})(\text{CO})_2(\text{MeCN})_2(\text{NCS})]$ (230 mg, 0.69 mmol) and 6,6'-dmbipy (143 mg, 0.78 mmol) reacted to afford **3** (109 mg, 36 %). ¹H NMR (400 MHz, CD_2Cl_2): δ 7.82 (3H, m), 7.38 (2H, d, $J = 8.4$ Hz), 7.24 (1H, s), 2.94 (6H, s), 2.62 (3H, m), 1.19 (2H, d, $J = 8$ Hz); (400 MHz, $(\text{CD}_3)_2\text{SO}$): δ 8.45 (2H, d, $J = 8$ Hz), 8.18 (2H, t, $J = 24$ Hz), 7.72 (2H, d, $J = 8$ Hz), 2.99 (6H, s), 2.90 (1H, m), 2.80 (2H, d, $J = 8$ Hz), 1.30 (2H, d, $J = 8$ Hz). IR (THF): $\nu(\text{CO})$ 1948, 1866 cm^{-1} ; $\nu(\text{CN})$ of NCS^- 2074 cm^{-1} .

X-ray Structure Determination. A crystal of $[\text{Mo}(\eta^3\text{-allyl})(\text{CO})_2(x,x'\text{-dmbipy})(\text{NCS})]$ was quickly mounted under Paratone-N oil and flash-cooled to 150 K in a stream of nitrogen in an Oxford Cryostream cooler. Single-crystal X-ray intensity data were collected using an Agilent Gemini S Ultra diffractometer (Mo $\text{K}\alpha$ radiation ($\lambda = 0.71073$ Å)). The data were reduced within the CrysAlisPro software.⁴⁷ The structure was solved using the program Superflip⁴⁸, and all non-hydrogen atoms were located. Least-squares refinements were carried out using the CRYSTALS suite of programs.⁴⁹ The non-hydrogen atoms were refined anisotropically. Each hydrogen atom of the ligands was placed geometrically with a C–H distance of 0.95 Å and a U_{iso} of 1.2–1.5 times the value of U_{iso} of the parent C atom. The positions of the hydrogen atoms were then refined with riding constraints. In the case of $[\text{Mo}(\eta^3\text{-allyl})(\text{CO})_2(6,6'\text{-dmbipy})(\text{NCS})]$, several disordered solvent molecules (DCM), which could not be modelled satisfactorily, were also present within the structure. The PLATON SQUEEZE software enabled the contribution to diffraction of the four disordered solvent molecules to be calculated, and thus it was possible to produce solvent-free diffraction intensities.⁵⁰ CCDC codes: **1** – 1862262; **2** – 1862263; **3** – 1862264.

Cyclic Voltammetry. Cyclic voltammograms were recorded on a PGSTAT 302N potentiostat (Metrohm Autolab) under an atmosphere of argon or carbon dioxide, using an air-tight three-electrode single-compartment cell. A Pt (128 μm) or Au (130 μm) disc microelectrode polished by a 0.25- μm diamond paste (Sommer) served as the working electrode; the counter and pseudo-reference electrodes were made of coiled Pt and Ag wires, respectively, protected by a glass mantle. Ferrocene (Fc) served as the internal reference, added just before the final potential scan. Occasionally, decamethylferrocene (Fc*) served for this purpose to avoid an overlap of the standard system with the nearby Mo(II)–NCS oxidation; $E_{1/2} = 0.48$ V vs Fc/Fc* (in THF). The CV samples contained 1 mM analyte and 0.1 M tetrabutylammonium hexafluorophosphate (TBAH) as the supporting electrolyte.

IR and UV-vis Spectroelectrochemistry. Infrared spectroelectrochemical experiments were performed on a Bruker 70v FT-IR spectrometer, equipped with either a DTLGS detector (measure-

ments at 298 K) or linked to an external Bio-rad FTS 60 MCT detector (measurements at 223 K). UV-Vis spectroelectrochemical experiments were conducted on a Scinco S-3100 diode array spectrophotometer. The electrochemical response in the form of a thin-layer cyclic voltammogram (TL-CV) at $\nu = 2 \text{ mV s}^{-1}$ was recorded during both IR and UV-vis monitoring of the controlled-potential electrolysis with an EmStat3 potentiostat (PalmSens). The spectroelectrochemical measurements were conducted with an optically transparent thin-layer electrochemical (OTTLE) cell (Spectroelectrochemistry Reading) in the room-temperature⁵¹ and the cryostated low-temperature⁵² versions. Both OTTLE cells were equipped with a Pt minigrad working electrode, a Pt minigrad counter electrode, an Ag wire pseudo-reference electrode and CaF_2 windows. The room-T OTTLE cell was also used with an Au minigrad working electrode. The SEC samples contained 3 mM analyte and 0.3 M TBAH.

Computational studies. Density Functional Theory calculations⁵³ were performed, using the Amsterdam Density Functional program (ADF).⁵⁴⁻⁵⁶ Geometries were optimized with gradient correction, without symmetry constraints, using the Local Density Approximation of the correlation energy (Vosko-Wilk-Nusair)⁵⁷ and the Generalized Gradient Approximation (Becke's⁵⁸ exchange and Perdew's^{59,60} correlation functionals). Unrestricted calculations were carried out for open-shell complexes. Solvent was considered in all geometry optimizations and single-point calculations in accordance with the COSMO approach were implemented in ADF. Tetrahydrofuran was always chosen, except for the PrCN-coordinated reduced complexes (Scheme 1) that were modelled with acetonitrile. Relativistic effects were treated with the ZORA approximation.⁶¹ Triple- ζ Slater-type orbitals (STO) were used to describe all the valence electrons of H, O, C, N, S, and Mo. A set of two polarization functions was added to H (single- ζ 2s, 2p), O, C, N, S (single- ζ , 3d, 4f) and Mo (5d, 4f). Frequency calculations were carried out to obtain the vibrational spectra and to check that intermediates were minima in the potential energy surface. Time-Dependent DFT calculations⁶²⁻⁶⁵ with spin orbit coupling (SOPERT) were performed to determine the excitation energies.⁶⁶ The energy decomposition analysis (EDA)^{67,68} was performed on single-point calculations in the gas phase over the solvent-optimized geometries.

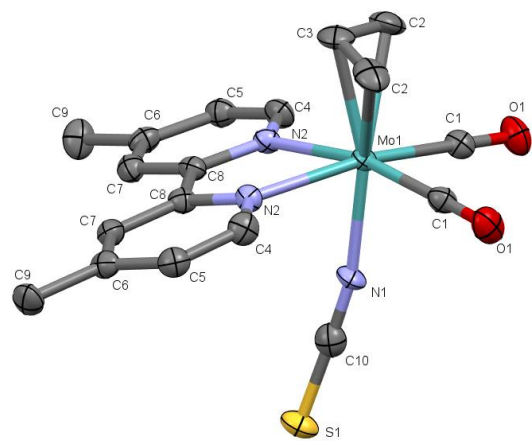
The X-ray structures described above were used for the calculations on parent x,x' -dmbipy complexes **1-3** and all the others were modelled after them. The more important isomers of each species were considered, as well as different spin states when relevant. To check the effect of two possible isomers in solution, frequencies and absorption spectra were calculated for both, and the differences were much smaller than differences to other complexes of the same ligand. Three-dimensional representations of the structures and molecular orbitals were obtained with Chemcraft.⁶⁹

RESULTS AND DISCUSSION

Characterization and Crystal Structure Analysis. Infrared spectra of dicarbonyl complexes **1-3** show the two $\nu(\text{CO})$ absorption bands close to 1950 and 1870 cm^{-1} (Table 2). Compared with the $\nu(\text{CO})$ modes of the unsubstituted-bipy reference, $[\text{Mo}(\eta^3\text{-allyl})(\text{CO})_2(\text{bipy})(\text{NCS})]$, the wavenumbers of **1-3** do not deviate significantly, reflecting the limited electronic effect of the methyl substitution on the CO π -back-donation. The two CO-stretching wavenumbers are almost identical for **2** and only slightly smaller for **1**. The largest $\nu(\text{CO})$ drop in the series (up to 5 cm^{-1}) is caused by the inductive effect of the donor methyl substituents at 6,6'-dmbipy. The $\nu(\text{CN})$ mode of the axial thiocyanato ligand in **1** and **2** also remains positioned near 2080 cm^{-1} (in PrCN) and 2075 cm^{-1} (in THF) compared to

the reference bipy complex. The CO π -back-donation increases, and thiocyanate π -donation decreases at lower temperatures, both in PrCN and THF.

The crystal structures of **1-3** (shown in Figure 1 for **1** and **3**, and Figure C-S1 (Supporting Information) for **2**) reveal that these complexes all adopt the type A pseudo-octahedral structure encountered in most $[\text{M}(\eta^3\text{-allyl})(\text{CO})_2(\text{L}\text{O}\text{L})\text{X}]$ complexes (L OL = chelating bidentate ligand, X = monodentate anionic ligand), including $[\text{Mo}(\eta^3\text{-allyl})(\text{CO})_2(\text{bipy})(\text{NCS})]$,⁷⁰ also known as the equatorial isomer. The type A structure is symmetric, characterized by both L OL donor atoms appearing in the trans position to the carbonyl ligands, defining the equatorial plane. The less symmetric type B structure (axial isomer), where the η^3 -allyl and one CO ligand are trans to the L OL donor atoms, is only seen in rare instances⁷¹⁻⁷⁴, but is particularly common for larger, more sterically-hindered donor ligands or those with strong π -accepting properties such as the 2,6-xylyl-BIAN (= bis(2,6-dimethylphenyl)-acenaphthenequinonediimine) ligand.^{45,74} As is found in practically all the complexes in this family, the open face of the allyl ligand in **1-3** lies over the equatorial CO ligands. While almost linear in the reference bipy complex⁶⁹, the structure of the NCS⁻ ligand is bent in the dmbipy complexes, toward the 4,4'-dmbipy ligand in **1**, while away from the 6,6'-dmbipy ligand in **3**, forced by packing interactions (Figure 1). The bond angle between the equatorial CO ligands is compressed in **3** (76°) relative to **1** (82°). In the reference bipy complex, this angle is 78°, the mid-way point between the two extremes.⁶⁹ In addition to this, the two rings in chelated 6,6'-dmbipy in **3** are not co-planar, but have a dihedral angle around the NCCN moiety of -7.2°. In **1**, the corresponding angle is 0°. These observations indicate that the methyl groups in the 6,6'-positions exert a stronger steric impact over the rest of the complex. Corresponding crystallographic data for **1-3** are presented in Tables C-S1 and C-S2 (Supporting Information).



dmbipy)(NCS)] (**3**, bottom) determined by single-crystal X-ray analysis. Hydrogen atoms have been omitted for clarity.

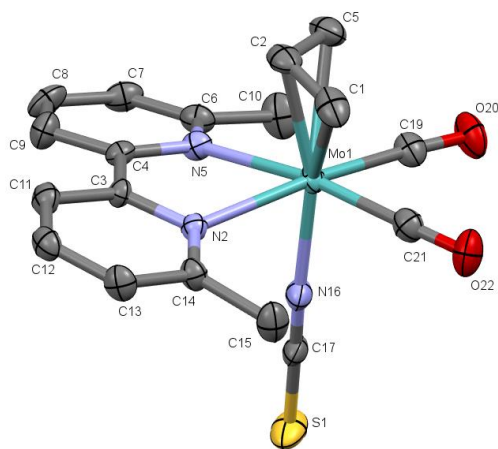


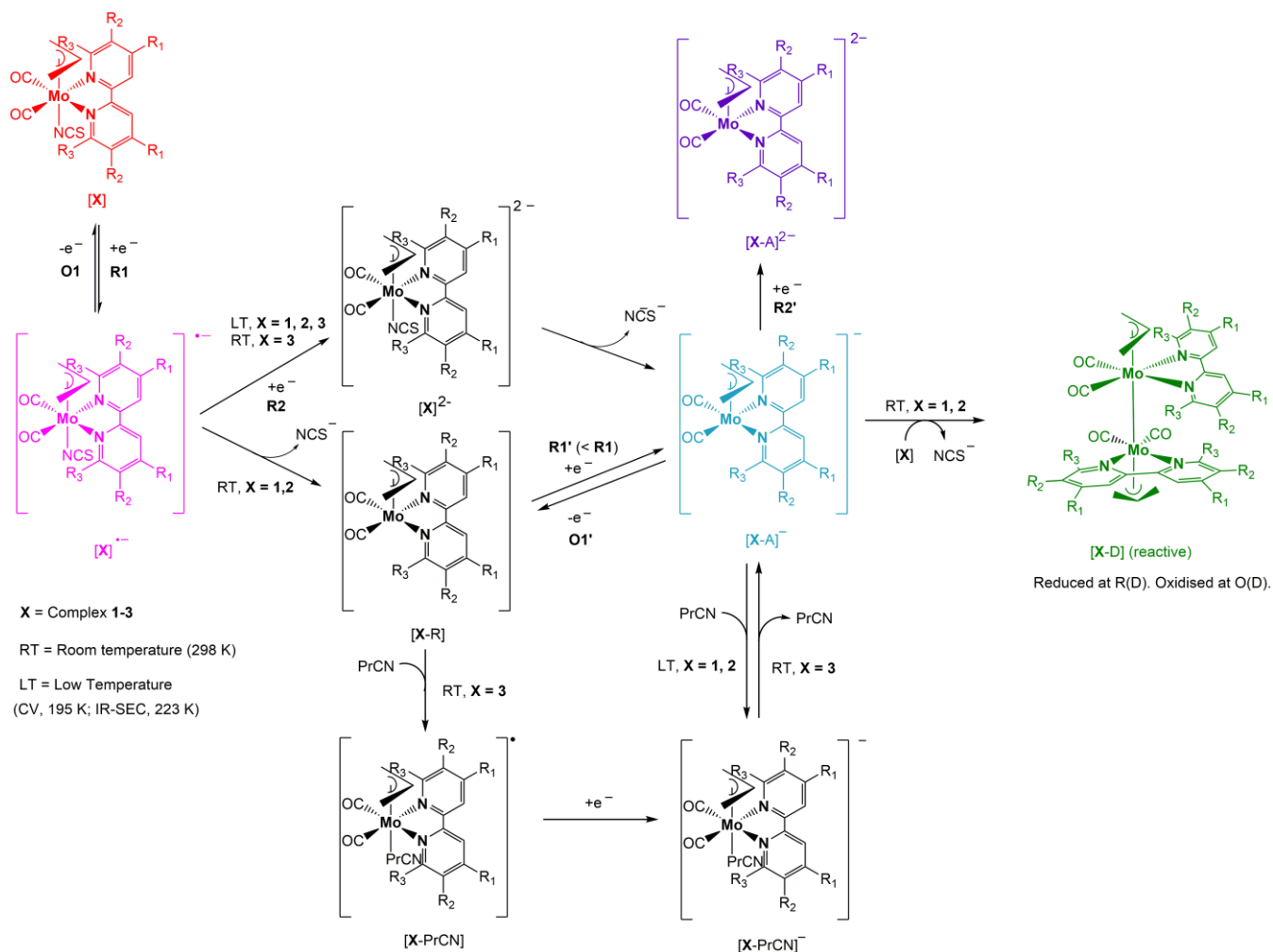
Figure 1. An ORTEP view (50% thermal probability) of molecular structures of [Mo(η^3 -allyl)(CO)₂](4,4'-dmbipy)(NCS)] (**1**, top) and [Mo(η^3 -allyl)(CO)₂](6,6'-

Table 1. Redox potentials (V vs Fc/Fc⁺) of complexes **1 and **3** and their reduction products (see Scheme 1) from cyclic voltammetry at an Au microdisc electrode at 298 K. Table E-S1 (Supporting Information) presents the complete list, including the data for complex **2**.**

Complex	Solvent	Mo(II/III) $E_{1/2}$	R1 $E_{p,c}$	R2 $E_{p,c}$	R2' $E_{p,c}$	O1' $E_{p,a}$	R(D) $E_{p,c}$	O(D) $E_{p,a}$
[Mo(η^3 -allyl)(CO) ₂ (bipy)(NCS)] ^c	THF	0.20	-1.99	-	-2.82	-1.74	-2.52	<i>e</i>
	PrCN	0.22	-1.95	-2.59	-2.77	-1.74	<i>e</i>	-0.80
	PrCN ^b	<i>d</i>	-1.88 ^a	-2.58 ^b	<i>f</i>	-1.58	<i>e</i>	-0.63
[Mo(η^3 -allyl)(CO) ₂ (4,4'-dmbipy)(NCS)] (1)	THF	0.18	-2.06	-	-2.78	-1.82	-2.46	-1.18
	THF ^b	0.22	-1.96 ^a	-2.53	-2.80 ^a	-1.68	<i>e</i>	-1.17
	PrCN	0.22	-1.99	-	<i>f</i>	-1.74	-2.36	<i>e</i>
	PrCN ^b	0.22	-1.96 ^a	-2.55	<i>f</i>	-1.54	<i>e</i>	-1.16
[Mo(η^3 -allyl)(CO) ₂ (6,6'-dmbipy)(NCS)] (3)	THF	0.26	-2.02 ^a	-2.57	-2.94	-1.84	-	-
	THF ^b	0.28	-1.98 ^a	-2.60	-2.82 ^a	-1.66	-	-
	PrCN	0.32	-1.93 ^a	-2.45	<i>f</i>	-1.73	-	-
	PrCN ^b	0.28	-1.94 ^a	-2.56	<i>f</i>	-1.54	-	-

^a $E_{1/2}$ value (anodic counter wave observed). ^b Measured at 195 K. ^c The reference complex, measured at a Pt electrode.⁴⁵ ^d Not measured. ^e Not observable. ^f Beyond the accessible cathodic potential window of PrCN/TBAH.

Scheme 1 General cathodic pathways of complexes **1-3** (= **X**) based on the evidence from cyclic voltammetry (colored molecular structures). The evidence for radical $[X\text{-PrCN}]$ and anion $[X\text{-PrCN}]^-$ ($X = 1$ and 2) comes solely from IR spectroelectrochemistry.



Color scheme: red - parent complex; pink - corresponding one-electron-reduced radical anion; blue - two-electron-reduced five-coordinate anion; green - one-electron-reduced dimer (tentative structure); purple - three-electron-reduced five-coordinate dianion.

DFT calculations⁵³ using the ADF program⁵⁴⁻⁵⁶ were performed on **1-3** in order to understand the role of the methyl substituents and to calibrate the method to identify the species detected in the spectro-electrochemical experiments. The equatorial isomer is indeed always preferred, the energy difference increasing as the methyl substituents approach the metal - 0.67, 0.86, and 5.45 kcal mol⁻¹ for **1**, **2**, and **3**, respectively (Tables DFT-S1 and DFT-S2, Supporting Information). Substituents in adjacent positions to the donor N-atoms give rise to a distortion of the coordinated dmbipy ligand in the equatorial isomer (Figure 1) but lead to severe repulsion with the allyl hydrogen atoms. This is reflected in the binding energy of each dmbipy to the {Mo(η^3 -allyl)(CO)₂(NCS)} fragment, which is ~41 kcal mol⁻¹ for **1** and **2**, but only 33 and 27 kcal mol⁻¹ for the equatorial and axial isomers of **3**. The structural parameters are well reproduced (Tables DFT-S3 and C-S2, Supporting Information).

A fragment decomposition analysis helps to understand the origin of the lower binding energy of the 6,6'-dmbipy ligand

compared to the 4,4'- and 5,5'-derivatives (Table DFT-S4, Supporting Information). Indeed, the ca. 8 kcal mol⁻¹ difference results from two sources. The first one is the extra energy needed to distort the fragments from their optimized geometry to the geometry they have in the complex. The Mo fragment requires ca. 0.5 kcal mol⁻¹, and the dmbipy ligands ca. 2.5 kcal mol⁻¹. The second contribution is the loss of covalent interaction between the two fragments (ca. 5 kcal mol⁻¹). These intrinsic differences will play a role in the reactivity of the complexes.

Cyclic Voltammetry. Cyclic voltammetry of **1-3** was conducted at room (298 K) and low (195 K) temperatures at an Au microdisc electrode in argon-saturated THF/TBAH (Figures 2-4) and PrCN/TBAH (Figures E-S1 - E-S3, Supporting Information). Reference measurements at a Pt microdisc electrode are depicted in Figures E-S4 - E-S6 (THF) and E-S7 - E-S9 (PrCN), Supporting Information. The redox potentials obtained for **1** and **3** with the Au microdisc are summarized in Table 1. For complex **2** these data are available in complete Table E-S1 (Supporting Information). Redox potentials measured in the

series **1-3** on a Pt microdisc are summarised in Table E-S2 (Supporting Information).

The redox behavior of **1** closely resembles that reported⁴⁵ for the reference complex $[\text{Mo}(\eta^3\text{-allyl})(\text{CO})_2(\text{bipy})(\text{NCS})]$. In the anodic region, **1** undergoes reversible, formally Mo-based $1e^-$ oxidation producing the cationic species $[\text{Mo}^{\text{III}}(\eta^3\text{-allyl})(\text{CO})_2(4,4'\text{-dmbipy})(\text{NCS})]^+$, even in strongly coordinating PrCN. This result proves that the donor ability of the dmbipy ligand is sufficient to stabilize the higher oxidation state. Despite this, the influence of the methyl substituents on the actual anodic potential is negligible. On the slow cathodic scan at $\nu = 100 \text{ mV s}^{-1}$, **1** undergoes irreversible dmbipy-based reduction to $\mathbf{1}^{\bullet-}$, in weakly coordinating THF at $E_{p,c} = -2.06 \text{ V}$ (R1 in Figure 1). In PrCN, this irreversible process occurs less negatively at $E_{p,c} = -1.99 \text{ V}$. Reversing the scan direction just behind the initial cathodic wave in either solvent exposes a nearby irreversible anodic wave at $E_{p,a} = -1.82 \text{ V}$ (THF) or $E_{p,a} = -1.92 \text{ V}$ (PrCN); this process is designated O1'. From a comparison with both the reference bipy complex and the cathodic cyclic voltammogram of $[\text{Mn}(\text{CO})_3(\text{bipy})\text{Br}]^{22}$, O1' can be assigned to the oxidation of the 5-coordinate anion $[\text{Mo}(\eta^3\text{-allyl})(\text{CO})_2(4,4'\text{-dmbipy})]^-$ ($[\mathbf{1-A}]^-$ in Scheme 1), classifying the initial reduction at R1 as a formally $2e^-$ process. The initial $1e^-$ reduction of **1** forms unstable $\mathbf{1}^{\bullet-}$ that readily loses the axial monodentate ligand NCS⁻ (see the Spectroelectrochemical section for support) and converts to the corresponding 5-coordinate radical, $[\text{Mo}(\eta^3\text{-allyl})(\text{CO})_2(4,4'\text{-dmbipy})]$ ($[\mathbf{1-R}]$) readily reducible at $R1' < R1$ (ECE) to $[\mathbf{1-A}]^-$. This 5-coordinate anion is detectable by its irreversible oxidation at O1' but also its $1e^-$ reduction to $[\text{Mo}(\eta^3\text{-allyl})(\text{CO})_2(4,4'\text{-dmbipy})]^{2-}$ ($[\mathbf{1-A}]^{2-}$) at R2' (becoming reversible at 195 K, $E_{1/2} = -2.80 \text{ V}$ (THF)), similar to the redox behavior of $[\text{Mn}(\text{CO})_3(\text{bipy})]^-$ under argon.²² The wave R2' was poorly resolved in PrCN at the edge of the accessible potential window.

The new cathodic wave R(D) in the room-temperature CV of **1**, observed at $E_{p,c} = -2.46 \text{ V}$ (in THF) and -2.36 V (in PrCN), can be attributed to the reduction of the Mo–Mo bonded dimer $[\text{Mo}(\eta^3\text{-allyl})(\text{CO})_2(4,4'\text{-dmbipy})]_2$ ($[\mathbf{1-D}]$ in Scheme 1) formed on the selected time scale from the unreduced parent complex by its electron-transfer reaction with $[\mathbf{1-A}]^-$ electrogenerated at R1 by the irreversible ECE process. The reduction of $[\mathbf{1-D}]$ appears reversible on the CV time scale of seconds; although, ultimately it should reproduce $[\mathbf{1-A}]^-$. This route has been reported for reference $[\text{Mn}(\text{CO})_3(\text{bipy})]_2$.²² However, $[\mathbf{1-D}]$ exhibits inherent secondary reactivity, revealed by IR spectroelectrochemistry in the following section, preventing us to obtain a clear spectroscopic evidence for this process. The oxidation of $[\mathbf{1-D}]$ is visible on the reverse anodic scan in THF as a weak anodic wave O(D) at $E_{p,a} = -1.17 \text{ V}$, beyond the oxidation of $[\mathbf{1-A}]^-$ at O1' that triggers the ECEC dimerization process similar to that at R1 via 5-coordinate radical $[\mathbf{1-R}]$ (Scheme 1). The latter species probably binds back the liberated NCS⁻ ligand; the concomitant oxidation (O1' < O1) reproduces parent **1** that reacts with yet non-oxidized $[\mathbf{1-A}]^-$ to form dimer $[\mathbf{1-D}]$ detected more positively by its oxidation at O(D). Differently from the cathodic dimerization route, the donor solvent (especially PrCN) may play a role in the intimate mechanism of the anodic dimerization.

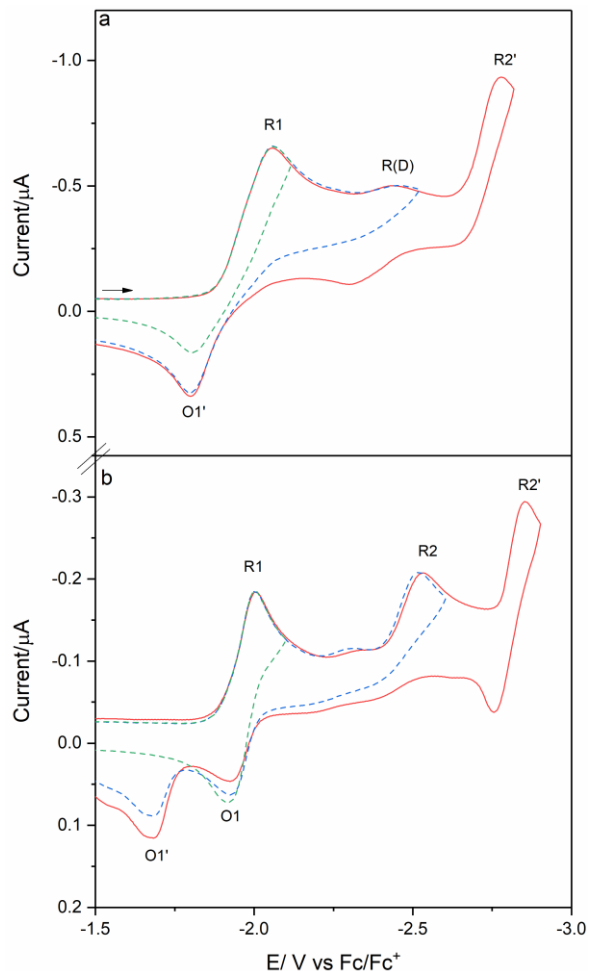


Figure 2. Cyclic voltammetry of $[\text{Mo}(\eta^3\text{-allyl})(\text{CO})_2(4,4'\text{-dmbipy})(\text{NCS})]$ (**1**), in THF/TBAH (a) at room temperature and (b) 195 K. Scan Rate: 100 mV s^{-1} . Au microdisc electrode. The arrow indicates the initial scan direction.

At sufficiently low temperatures, parent radical anion $[\mathbf{1}]^{\bullet-}$ formed at R1 becomes stable, resulting in a reversible R1/O1 couple, $E_{1/2} = 1.93 \text{ V}$ (THF, Figure 1) or -1.96 (PrCN, Figures E-S1 and E-S7, Supporting Information). $[\mathbf{1-A}]^-$ is then formed only at the newly observed irreversible cathodic wave R2, $E_{p,c} = -2.53 \text{ V}$ (THF) or -2.55 (PrCN), upon rapid dissociation of NCS⁻ from 6-coordinate $[\mathbf{1}]^{2-}$. The quasi-reversible reduction of $[\mathbf{1-A}]^-$ to 5-coordinate dianion occurs again at R2', $E_{p,c} = -2.85 \text{ V}$ (THF). Compared to room-temperature CV, the reverse oxidation of $[\text{Mo}(\eta^3\text{-allyl})(\text{CO})_2(4,4'\text{-dmbipy})]^-$ is shifted upon cooling more positively ($>100 \text{ mV}$) from the parent reduction at R1. The anodic ECEC dimerization process is observable at low temperatures only in THF (a minor O(D) wave at -1.17 V).

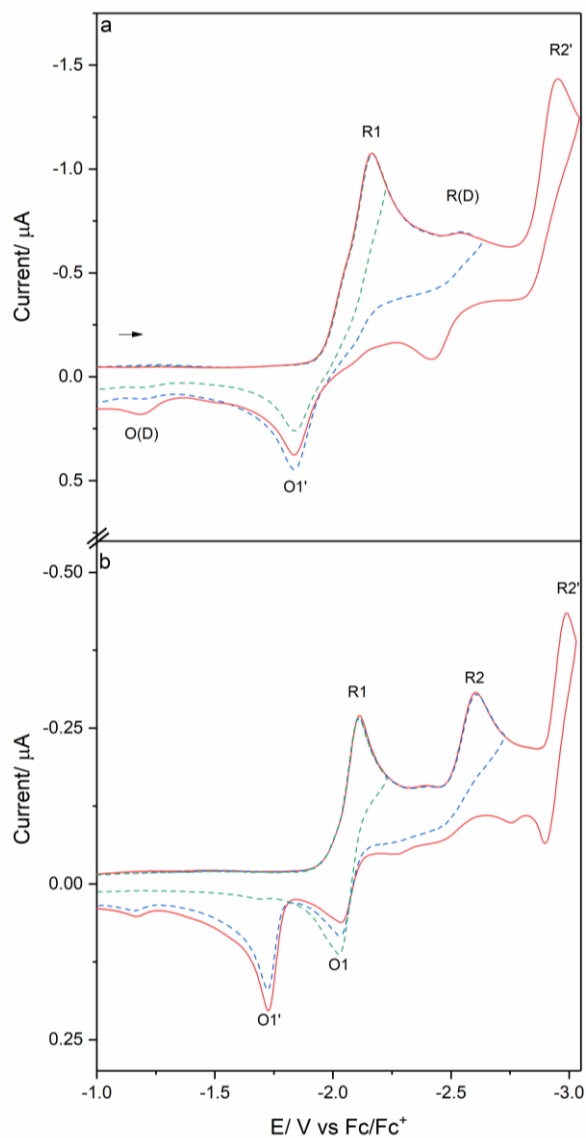


Figure 3. Cyclic voltammetry of $[\text{Mo}(\eta^3\text{-allyl})(\text{CO})_2](5,5'\text{-dmbipy})(\text{NCS})$ (**2**) in THF/TBAH at (a) room temperature and (b) 195 K. Scan rate: 100 mV s^{-1} . Au microdisc electrode.

The analysis of the redox behavior of **2** under ambient conditions (Figure 3 (THF) and Figures E-S2 and E-S8, Supporting Information (PrCN)) leads to a description that is largely comparable to that of **1** (Table 1, Tables ES-1 and E-S2 (Supporting Information), and Scheme 1), with only minor differences in the electrode potential values of each redox process. It is noteworthy that the reference complex $[\text{Mo}(\eta^3\text{-allyl})(\text{CO})_2(\text{bipy})(\text{NCS})]$ with the less donating bipy ligand⁴⁵ showed a partially reversible reduction to the corresponding radical anion at R1 in PrCN at room temperature already at $\nu = 100 \text{ mV s}^{-1}$ while the radical anions of **1** and **2** are more reactive and not observable under the same experimental condition, as revealed by the absent counter wave O1.

The redox behavior of **3** (Figure 4, and Figures ES-3 and E-S9, Supporting Information) strongly differs from that of **1** and **2**. The formally metal-based oxidation becomes quasi-reversible and markedly positively shifted to $E_{1/2} = 0.26 \text{ V}$ (THF) or 0.32 V (PrCN); the anodic potential in PrCN is more positive by

100 mV than that of the reference complex with the unsubstituted bipy ligand, whereas complexes **1** and **2** oxidize at slightly less positive potentials (Table 1, and Tables E-S1 and E-S2, Supporting Information). In the cathodic range, the reduction of parent **3** at R1 to radical anion $\mathbf{3}^{\cdot-}$ at $E_{1/2} = -2.03 \text{ V}$ (THF) or -1.93 V (PrCN) is reversible at $\nu = 100 \text{ mV s}^{-1}$ already at room temperature (Figure 4). This difference has several implications for following cathodic path. Unlike **1** and **2**, there is no evidence for the formation (absent O1') of 5-coordinate anion $[\mathbf{3-A}]^-$ until the irreversible wave R2 at $E_{p,c} = -2.57 \text{ V}$ (THF) or -2.45 V (PrCN) is passed, where the latter is directly produced by NCS^- dissociation from the transient six-coordinate dianion. On the reverse anodic scan initiated beyond R2, the anodic wave O1' is clearly seen at $E_{p,a} = -1.84 \text{ V}$ (THF) or -1.73 V (PrCN). The absence of $[\mathbf{3-A}]^-$ at R1 prevents also the formation of dimer $[\mathbf{3-D}]$, which is reflected in the absence of its R(D) and O(D) signatures. The absent anodic wave O(D) indicates that the dimerization reaction between $[\mathbf{3-A}]^-$ and parent **3** (reformed at O(D)) is inhibited. The 5-coordinate anion is further reduced to $[\mathbf{3-A}]^{2-}$ at R2', $E_{p,c} = -2.94 \text{ V}$ (THF). At low temperatures, R2' takes on the reversible character and slightly shifts to $E_{1/2} = -2.82 \text{ V}$ (Figure 4(b)).

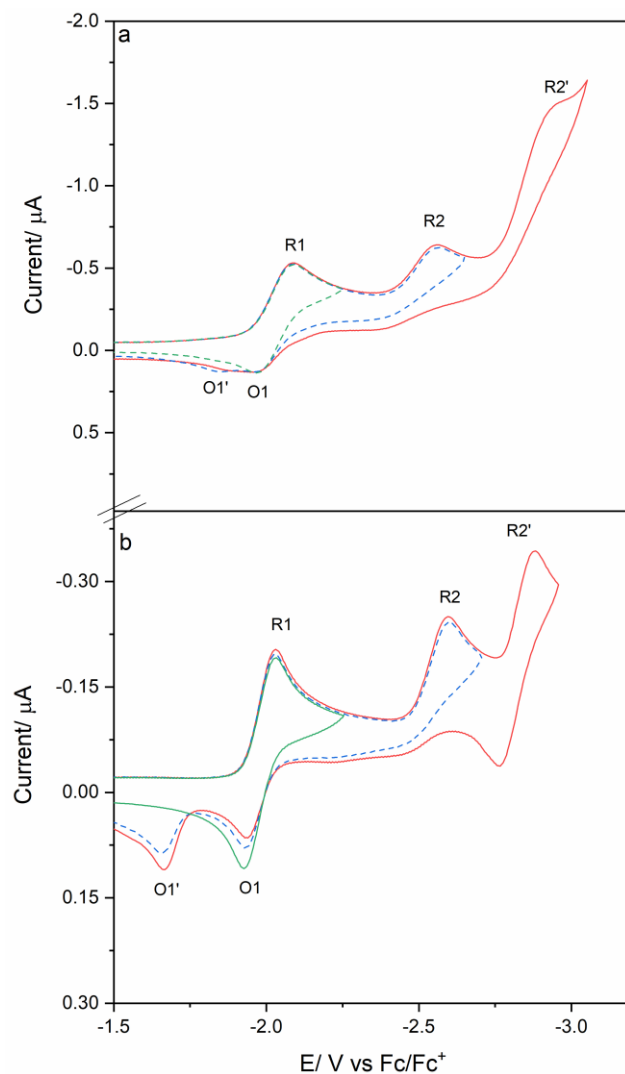


Figure 4. Cyclic voltammery of $[\text{Mo}(\eta^3\text{-allyl})(\text{CO})_2(6,6'\text{-dmbipy})(\text{NCS})]$ (**3**), in THF/TBAH (a) at room temperature and (b) 195 K. Scan Rate: 100 mV s^{-1} . Au microdisc electrode.

On electronic grounds, the addition of methyl groups to bipy in the 4,4'-positions (**1**) and 5,5'-positions (**2**) increases electron donation toward the $\text{Mo}\cap\text{bipy}$ metallacycle and the axial Mo-NCS bond, as evidenced by the more negative reduction potentials, destabilizing the corresponding radical anions compared to the reference complex with 2,2'-bipyridine. The magnitude of the R1 potential shift is comparable to that reported for $[\text{Mo}(\text{CO})_4(x,x'\text{-dmbipy})]$ ($x = 4\text{-}6$) and $[\text{Re}(\text{CO})_3(x,x'\text{-dmbipy})\text{Cl}]$ ($x = 3\text{-}5$) vs their respective bipy counterparts.^{39,75} The redox behavior following the donor substitution in the 6,6'-position (**3**) is extremely unusual, resulting in the apparently stable radical anion formed upon $1e^-$ reduction. In addition, it also stabilizes $[\mathbf{3-A}]^-$ and hinders the follow-up dimerization involving this $2e^-$ reduced species and parent **3**. A similar inhibiting effect on the dimerization was reported by Kubiak and co-workers for $[\text{Mn}(\text{CO})_3(6,6'\text{-dimesityl-bipy})]^-$ stabilized by the large substituents in the vicinity of the $\text{Mn}\cap\text{bipy}$ metallacycle.²⁵

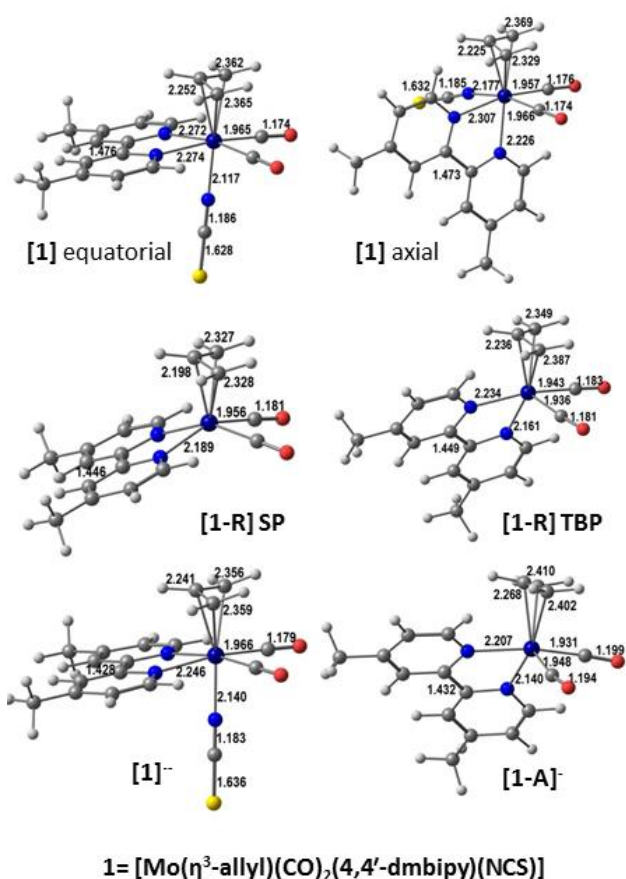


Figure 5. DFT-optimized structures of the parent complex $[\text{Mo}(\eta^3\text{-allyl})(\text{CO})_2(4,4'\text{-dmbipy})(\text{NCS})]$, **1** (the equatorial isomer (top left) and the axial isomer (top right)), $1e^-$ reduced radical anion $[\mathbf{1}]^-$ (bottom left), 5-coordinate radical $[\mathbf{1-R}]$ (the SP isomer (left) and the TBP isomer (right)), and $2e^-$ reduced 5-coordinate anion $[\mathbf{1-A}]^-$ (bottom right), with the relevant bond lengths (Å).

Computational Studies. The behavior of **1-3** upon electrochemical reduction, and the nature of the reduction products

formed, as revealed by the preceding CV studies, were investigated in detail with quantum chemical calculations (Amsterdam Density Functional).⁵⁴⁻⁵⁶ Their initial $1e^-$ reduction of **1-3** leads to the formation of corresponding radical anions; only $\mathbf{3}^-$ has been found sufficiently stable at ambient conditions (Figure 4). The geometry optimization (Table DFT-S2, Supporting Information) reveals that the axial isomer is preferred for $[\mathbf{1}]^-$ and $[\mathbf{2}]^-$ by less than 1 kcal mol^{-1} , while the less strained equatorial form remains significantly favored by $[\mathbf{3}]^-$ (ca. 6 kcal mol^{-1}). The binding energy of the NCS^- ligand in each anion is 7.8 ($[\mathbf{1}]^-$), 6.8 ($[\mathbf{2}]^-$), and 10.74 ($[\mathbf{3}]^-$) kcal mol^{-1} , suggesting that thiocyanate will be less easily released by $[\mathbf{3}]^-$, in line with the CV observations. The effect of the reduction on the structure is observed in the shortening of the central C1-C1' bond of the bidentate ligand (from 1.476 to 1.428 \AA in **1**), reflecting the dominant localization of the complex LUMO on x,x' -dmbipy, and in the lengthening of the carbonyl C-O distances (Figure 5, and Figures DFT-S1 and DFT-S2, Supporting Information).

The HOMO of **1** (Figure 6) is bonding between the metal and the π -acceptor carbonyls and allyl, but π -antibonding between Mo and the axial π -donor thiocyanate, being mainly a Mo orbital. Hence, the $1e^-$ oxidation of **1-3** can formally be $\text{Mo}^{\text{II}} \rightarrow \text{Mo}^{\text{III}} + e^-$. Strong σ -donation from x,x' -dmbipy ($x = 4\text{-}6$) is therefore needed to stabilize $[\mathbf{1}]^+ \text{-} [\mathbf{3}]^+$, as observed (see the following SEC section). The LUMO and LUMO+1 of **1** are largely localized on 4,4'-dmbipy, both being bonding between C1 and C1'. Shortening of this distance is therefore expected upon the reduction.

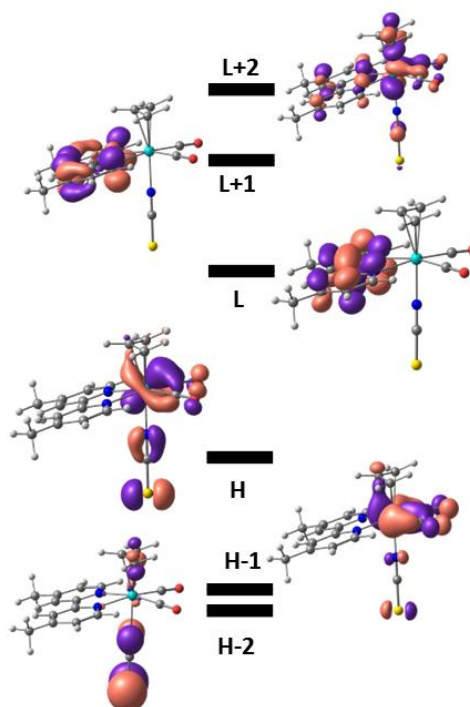


Figure 6. DFT-calculated frontier orbitals in the parent complex $[\text{Mo}(\eta^3\text{-allyl})(\text{CO})_2(4,4'\text{-dmbipy})(\text{NCS})]$, **1**. The HOMO-LUMO (H-L) gap is 1.574 eV .

The identification of the diverse carbonyl complexes formed along the cathodic pathways can be most effective by analysis of the vibrational stretching modes of the CO ligands (Table DFT-S5, Supporting Information). The calculated wavenumbers are practically independent of the methyl substitution pattern. The absorption maxima of the symmetric and antisymmetric modes for **1**, **2** and **3** lie at 1882, 1883, 1881 cm^{-1} and at 1800, 1801, 1800 cm^{-1} , respectively. Frequency calculations need a scaling factor to reproduce experimental values. These calculated values are ca. 0.97 of the experimental ones, in a very good agreement. Interestingly, the trend in the neutral and singly reduced species is the same (the largest wavenumbers found for **2**). In THF, the experimental wavenumbers for **1** and **[1]⁻** are 1949, 1869 cm^{-1} and 1926, 1815 cm^{-1} , respectively (Table 2, in the following section). Application of the 0.97 factor converts them to 1891, 1813 cm^{-1} and 1868, 1760 cm^{-1} , respectively; these values are very close to those calculated in Table DFT-S5 (Supporting Information).

Electronic absorption of **1-3** in the visible spectral region, having a charge-transfer character, was investigated with TDDFT calculations and the results are presented in Supporting Information (see Table DFT-S6 and the accompanying text). The calculated frontier molecular orbitals of **1-3** are shown in Figure 6, and Figures DFT-S3 and DFT-S4 (Supporting Information), respectively.

The concomitant loss of the thiocyanate anion from the initial radical anion will afford the transient 5-coordinate radicals $[\text{Mo}(\eta^3\text{-allyl})(\text{CO})_2(x,x'\text{-dmbipy})]$ ($x = 4-6$; **[X-R]** in Scheme 1). Their structure has been derived from both parent equatorial and axial isomers; this approach yielded geometries close to a square plane (SP) or a trigonal bipyramid (TBP), respectively. The latter was the most stable one by a negligible 0.4 kcal mol^{-1} for **[1-R]** and **[2-R]**, whilst the square-planar geometry was more strongly preferred for **[3-R]** (ca. 5 kcal mol^{-1}). Radical **[3-R]** was less stable than **[1-R]** and **[2-R]** by ca. 10 kcal mol^{-1} . The structure of **[1-R]** exhibits, for the two geometries calculated, larger carbonyl C–O and 4,4'-dmbipy inter-ring C–C bond lengths than calculated for **[1]⁻**, and smaller Mo–C(allyl) bond lengths (these are merely trends, the absolute differences are small, see Figure 5). These changes indicate that the loss of the NCS^- anion leads to stronger delocalization of the additional electron from the dominantly 4,4'-dmbipy radical anion in **[1]⁻** over the Mo-bis(carbonyl) unit in **[1-R]** (Figure 7).

Owing to their role in the reactivity characterizing the cathodic path, the frontier orbitals of **[1-R]**, as well as the spin density distribution in the 5-coordinate radical, are important. The orbitals of **[1-R]** are depicted in Figure DFT-S5 (Supporting Information). The spin density in the radicals is delocalized over the metal and the 4,4'-dmbipy ligand, with practically no contributions from the allyl and the carbonyls, as shown for **[1-R]** in Figure 7 (left), and for **[2-R]** and **[3-R]** in Figures DFT-S6 and DFT-S7 (Supporting Information), respectively.

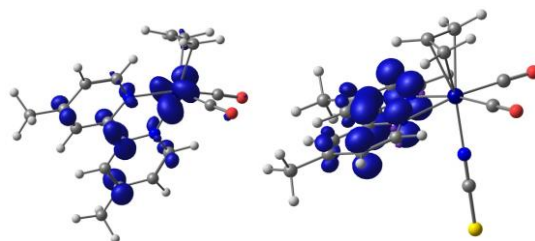


Figure 7. DFT-calculated spin density in the 5-coordinate radical $[\text{Mo}(\eta^3\text{-allyl})(\text{CO})_2(4,4'\text{-dmbipy})]$, **[1-R]** (left), and precursor 6-coordinate radical anion **[1]⁻** (right).

The direct $1e^-$ reduction of 5-coordinate radicals **[X-R]** (**X** = **1**, **2**, **3**), formed at the irreversible cathodic wave R1 (Figure 1(a)), produces 5-coordinate anions **[X-A]⁻** that may in principle exist in closed-shell singlet or open-shell triplet states. As expected, the former alternative is more stable in all the three cases, by 16.9 and 19.2 kcal mol^{-1} for **[1-A]⁻** and **[2-A]⁻**, but by only 11.8 kcal mol^{-1} for **[3-A]⁻**, emphasizing again the differences exhibited by the 6,6'-dmbipy derivatives. The addition of the second electron leads to longer Mo–C(allyl) bonds compared not only to precursors **[X-R]** but also to neutral parent compounds **X**, suggesting a possible allyl loss opening a decomposition pathway. The C–O bonds lengthen, while the C–C inter-ring bond in reduced x,x' -dmbipy shortens slightly. The structure of **[1-A]⁻** is shown in Figure 5; the others for **X** = **2** and **3** can be found in Figures DFT-S1 and DFT-S2 (Supporting Information), respectively.

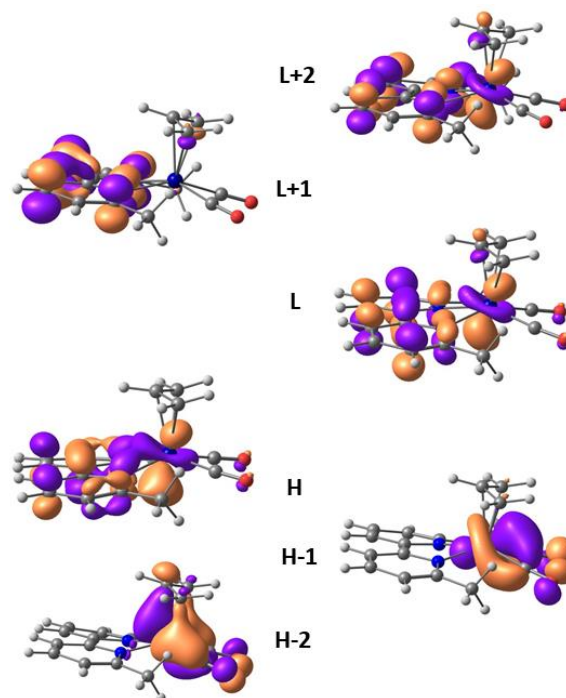


Figure 8. DFT-calculated frontier orbitals of the five-coordinate anion $[\text{Mo}(\eta^3\text{-allyl})(\text{CO})_2(6,6'\text{-dmbipy})]^-$, **[3-A]⁻**.

The calculated frequencies of parent **X** shift by 26–30 cm^{-1} for $\nu(\text{CO})_s$ and 37–40 cm^{-1} for $\nu(\text{CO})_a$ when reduction occurs and

radical anions $[X]^-$ are formed (Table DFT-S5, Supporting Information). Interestingly, the loss of the thiocyanate ligand has practically no effect on the stretching frequencies when going from $[3]^-$ to $[3-R]$ (less than 5 cm^{-1} for both modes). This effect on the π -back-donation to the carbonyl ligand is understandable, as the dissociation of the π -donor thiocyanate is compensated by the increased π -delocalization of the added electron from 4,4'-dmbipy to the $(\text{CO})_2\text{Mo-dmbipy}$ metallacycle. For the 4,4-dmbipy and 5,5'-dmbipy ligands, the consequence of the thiocyanate dissociation is not so small, since the $\nu(\text{CO})_s$ mode shifts by 7 and 5 cm^{-1} , respectively (for the axial geometry). As can be seen in Table DFT-S5 (Supporting Information), the reduction from the 5-coordinate radicals to the corresponding anions has more dramatic effects, the shifts reaching $\sim 90\text{ cm}^{-1}$ for the derivatives of **1** and **2**, and ~ 50 for cm^{-1} those of **3**. This difference testifies that the added second electron largely resides on the Mo dicarbonyl unit due to the extensive π -delocalisation of the frontier orbitals in $[X-A]^-$. This characteristic bonding property is clearly evidenced by the nature of the calculated frontier orbitals depicted in Figure 8 for $[3-A]^-$, and Figures DFT-S8 and DFT-S9 (Supporting Information) for $[1-A]^-$ and $[2-A]^-$, respectively. The strongly π -delocalized situation applies in all three cases for the HOMO and LUMO. The LUMO+1 and LUMO+2 are dominantly x,x' -dmbipy-localized while the HOMO-1 and HOMO-2 reside on the Mo-dicarbonyl unit. The molecular orbitals of the five-coordinate anions are indeed very similar in nature to those of the radical precursors (α orbitals), as can be seen for $[1-R]$ and $[1-A]^-$ in Figures DFT-S5 and DFT-S8 (Supporting Information), respectively.

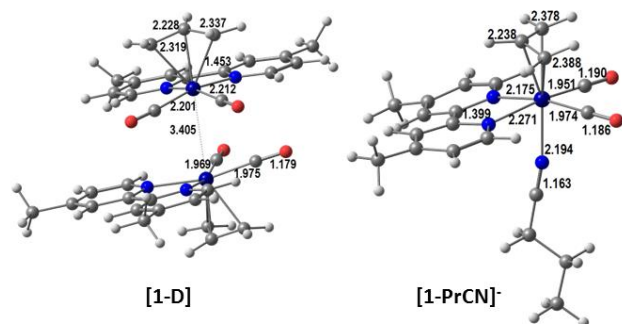


Figure 9. DFT-optimized structures of the 6-coordinate anion $[\text{Mo}(\eta^3\text{-allyl})(\text{CO})_2(4,4'\text{-dmbipy})(\text{PrCN})]^-$, $[1\text{-PrCN}]^-$ (the stable equatorial isomer (right)), and the staggered Mo–Mo dimer, $[1\text{-D}]$ (left), with relevant bond lengths (Å)

Two other reduced species are also formed, depending on the x,x' -dmbipy ligand. First, the existence of the 6-coordinate anion $[\text{Mo}(\eta^3\text{-allyl})(\text{CO})_2(4,4'\text{-dmbipy})(\text{PrCN})]^-$, $[1\text{-PrCN}]^-$, is not obvious from the preceding CV studies but a strong evidence for its participation comes from IR spectroelectrochemistry described in the following section. This low-temperature complex of PrCN and $2e^-$ reduced $[X-A]^-$ in the equatorial conformation was only observed for $[1\text{-PrCN}]^-$ (Figure 9) and $[2\text{-PrCN}]^-$ (Figure DFT-S10, Supporting Information); the absence of $[3\text{-PrCN}]^-$ (Figure DFT-S10, Supporting Information) may be explained by stronger stabilizing π -delocalization in the closer-to-square pyramidal structure of $[3-A]^-$ as well as by the steric hindrance by the adjacent methyl substituents. For $[1\text{-PrCN}]^-$, the axial and equatorial isomers, both as diamagnetic or paramagnetic species, were explored, but only the diamagnetic equatorial isomers could be calculated with PrCN coordinated in the original position of the thiocyanate ligand in parent **1** (Figure 9). The 4,4'-dmbipy inter-ring C–C distance of 1.399 Å

is significantly shorter compared to the values calculated for both diamagnetic $[1-A]^-$ (1.432 Å) and paramagnetic $[1]^-$ (1.426 Å) where 4,4'-dmbipy is considered to be formally $1e^-$ reduced. This may lead to the conclusion that both added electrons in $[1\text{-PrCN}]^-$ reside largely in the lowest $\pi^*(\text{dmbipy})$ orbital. On the other hand, the calculated wavenumbers of the $\nu(\text{CO})$ and PrCN $\nu(\text{CN})$ modes in $[X\text{-PrCN}]^-$ are still too low and too high, respectively, compared to the experimental values for stable 6-coordinate $[1\text{-PrCN}]^-$ (Table 2), which indicates only rather weak interactions of $[X-A]^-$ with PrCN, reflected also in positive binding energies with regard to the isolated components.

Five-coordinate radical and anionic species, $[X-R]$ and $[X-A]^-$, in the TBP geometry do not have obvious occupied frontier orbitals to form a Mo–Mo bond, but the SP conformers feature the SOMO and HOMO, respectively, with a strong contribution of $4d_{zz}$, as reflected in the orbital contour plots (Figure DFT-S11, Supporting Information, for $X = 1$). Therefore, it is easy to imagine two radicals forming a Mo–Mo bond, in $[1-D]$, by sharing electrons. This is equivalent to the formation of the dimer by the reaction between the $2e^-$ reduced anion and the neutral parent complex after the loss of the thiocyanate (via donation of $2e^-$ from $[1-A]^-$ to the empty orbital of **1**). Dimer $[1-D]$ obtained (Figure 9), displays a very long Mo–Mo bond but is a true intermediate (see the $\nu(\text{CO})$ wavenumbers in Table DFT-S5, Supporting Information). Other bond lengths are within normal values. A similar dimer could be obtained for **2** (Figure DFT-S10, Supporting Information). A definitive answer to the true nature of the dimer would require a more extensive analysis of possible alternatives and more experimental information.

The $2e^-$ reduction of **1** and **3** to corresponding 5-coordinate anions $[X-A]^-$ (Scheme 1) was also carried out under a CO_2 atmosphere, and there was an evidence of a different reactivity (see the following SEC section). Therefore, we used DFT calculations to look for derivatives of the 5-coordinated anion with CO_2 , both as equatorial and axial isomers of the adduct $[1\text{-CO}_2]^-$. The equatorial isomer (Figure 10) was more stable by 7.2 kcal mol^{-1} than the axial one (Table DFT-S1, Supporting Information).

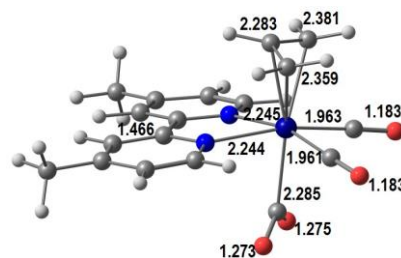


Figure 10. DFT-optimized structure of $[\text{Mo}(\eta^3\text{-allyl})(\text{CO})_2(4,4'\text{-dmbipy})(\text{CO}_2)]^-$, $[1\text{-CO}_2]^-$.

The narrow O–C–O angle in $[1\text{-CO}_2]^-$ of ca. 125° is consistent with a strong electronic reduction accompanying the coordination of CO_2 caused by the electron transfer from formally dianionic 4,4'-dmbipy seen, for example in $[1\text{-PrCN}]^-$. This is evidenced by a strong elongation of the C1–C1' inter-ring distance from 1.399 Å in the latter anion to 1.466 Å in $[1\text{-CO}_2]^-$. The latter value is very close to 1.476 Å for neutral 4,4'-dmbipy in **1**. The C=O bonds in the reduced CO_2 ligand are elongated to $1.273/1.275\text{ Å}$, which reflects their weakening. There is still significant electron density on the two carbonyl ligands, as revealed by the calculated CO-stretching wavenumbers of 1831

and 1714 cm^{-1} for the symmetric and asymmetric mode, respectively.

Infra-red and UV-vis absorption spectroelectrochemistry at low temperature. Molecular spectroelectrochemistry is commonly used in combination with conventional cyclic voltammetry (CV) to assign major redox products. In this work IR and UV-vis spectroscopy, in combination with thin-layer cyclic voltammetry (TL-CV), is very convenient to unravel the reduction paths of complexes **1-3** in association with the insight from the conventional cyclic voltammetry and the predictive power of the relevant DFT data in the preceding sections. The focus is placed on analysis of the IR stretching pattern and wavenumbers of the carbonyl ligands, the CN-stretching modes of the NCS⁻ and PrCN ligands, and the electronic absorption of the reduced x,x' -dmbipy ligands.

All three parent complexes are smoothly oxidized at 293 K to the corresponding stable (radical) cations. The corresponding CO- and CN-stretching wavenumbers and visible electronic absorption are summarized in Table E-S3 (Supporting Information). The IR spectral changes are supportive of the depopulation of the $\pi^*(\text{Mo-NCS})$ HOMO of the parent complexes, with a strong impact on the Mo-to-CO π -back-donation, strongly reduced in the formally Mo(III) products. It is important to note that the thermal stability of $[\mathbf{X}]^+$ is significantly higher compared to the cationic complex with the unsubstituted bipy ligand⁴⁵, proving the stronger donor ability of all three dimethylated x,x' -dmbipy ligand isomers. This result indicates that any major differences in the cathodic behavior of **1-3** should have their origin in the steric properties of the metallacycle imposed by the methyl substituents at x,x' -dmbipy ($x = 4-6$).

It is prudent to start the description of the cathodic behavior in the studied series of complexes with the low-temperature spectroelectrochemistry of **3** that displays arguably the most straightforward redox behavior, as revealed by cyclic voltammetry (Figure 4). This is because $[\text{Mo}(\eta^3\text{-allyl})(\text{CO})_2(6,6'\text{-dmbipy})(\text{NCS})]^-$ (**3⁻**) is perfectly stable in PrCN at low temperature; then, passing the reversible reduction step R1 at 223 K, only the radical anion is detected. The sole product is easily assignable from the distinctive high-energy shift of the $\nu(\text{CN})$ band of NCS⁻ from 2069 to 2089 cm^{-1} and the accompanying the low-energy shift of the two $\nu(\text{CO})$ bands from 1943 and 1859 cm^{-1} to 1919 and 1829 cm^{-1} , respectively (Figure 11(a)). These values show reasonable agreement with those procured from the DFT calculations (Table DFT-S5 (Supporting Information) and Table 2, scaling factor 0.97). The corresponding UV-vis-NIR spectral changes recorded during the initial reduction (Figure E-S10, Supporting Information) confirm the presence of the 6,6'-dmbipy radical anion in **3⁻** by its characteristic intra-ligand $\pi\pi^*$ absorption at 396 nm, bifurcated $\pi^*\pi^*$ at 489 and 518 nm, and low-lying $\pi^*\pi^*$ >600 nm^{37,76}, in line with the bipy-based LUMO of parent **3** (Figure DFT-S4, Supporting Information).

Radical anion **3⁻** was smoothly reduced in the following, irreversible $1e^-$ cathodic step at R2 generating the 5-coordinate anion $[\text{Mo}(\eta^3\text{-allyl})(\text{CO})_2(6,6'\text{-dmbipy})]^-$, [**3-A**]⁻ (Scheme 1). This process is recognized by the appearance of free NCS⁻ absorbing at 2050 cm^{-1} , and two low-lying broad $\nu(\text{CO})$ bands at 1797 and 1700 cm^{-1} , which are characteristic of a negatively charged dicarbonyl 5-coordinate species. The experimental

wavenumbers are in a very good agreement with the DFT values calculated for the equatorial square-pyramidal structure (Table 2) stabilized by strongly delocalized π -bonding in the metallacycle. It is the first time that reliable IR $\nu(\text{CO})$ values are reported for $2e^-$ reduced $[\text{Mo}(\eta^3\text{-allyl})(\text{CO})_2(a\text{-diimine})]^-$. In the published⁴⁵ pioneering work, the IR absorption of the more reactive anion $[\text{Mo}(\eta^3\text{-allyl})(\text{CO})_2(\text{bipy})]^-$ (detected by conventional cyclic voltammetry) was confused with products of thermal dimerization reactions (Scheme 1, and spectroelectrochemistry below). In the visible spectral region, [**3-A**]⁻ exhibits the characteristic absorption between 450-600 nm (Figure E-S11, Supporting Information) belonging to $\pi\pi^*$ electronic excitation⁷⁷ between the delocalized frontier orbitals of the Mo-dmbipy metallacycle (Figure 8).

In the preceding CV section, radical anions **1⁻** and **2⁻** were found to convert at ambient conditions within seconds to the corresponding five-coordinate anions already at the initial cathodic wave R1 (Figures 2(a) and 3(a), respectively). For **3⁻**, however, this ECE process is too slow to be detected on the CV time scale (Figure 4(a)). Therefore, the reduction of **3** at R1 and subsequent reactivity of its radical anion were studied by IR SEC at variable temperatures. At 223 K, **3⁻** remained stable. However, gradual temperature elevation to 273 K at the constantly applied cathodic potential R1 resulted in its complete conversion to $2e^-$ reduced [**3-A**]⁻ (Figure 12). This is the high-T ECE equivalent of the low-T EEC path at the cathodic potential R2 (Figure 11(b)). Reasons for the unusually high stability of **3⁻** are briefly discussed in the preceding DFT section.

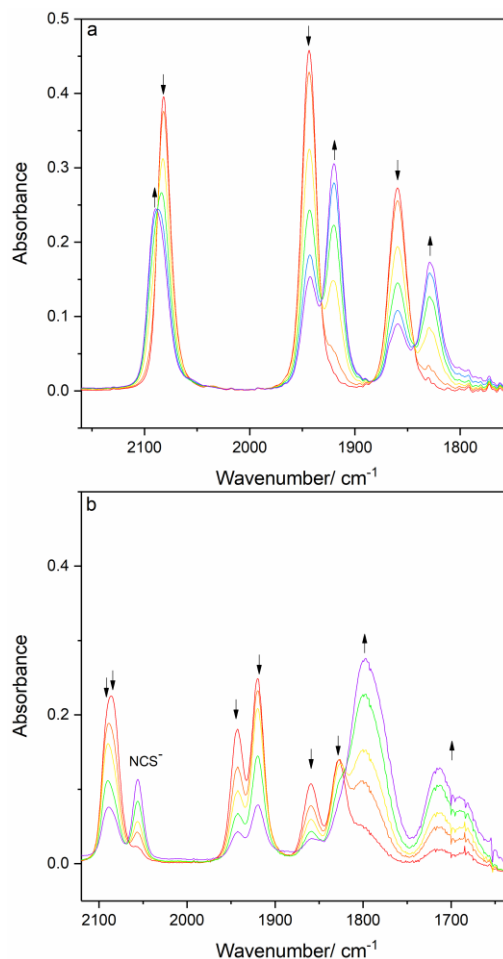


Figure 11. IR SEC monitoring of (a) the initial $1e^-$ reduction of $[\text{Mo}(\eta^3\text{-allyl})(\text{CO})_2(6,6'\text{-dmbipy})(\text{NCS})]$, **3** (\downarrow) at R1 to stable $3^{\bullet-}$ (\uparrow), and (b) the following reduction at R2 showing the conversion of $3^{\bullet-}$ to $[3\text{-A}]^-$ (\uparrow) and free NCS^- . Conditions: a cryostated OTTLE cell, PrCN/TBAH, 223 K.

Compared to **3**, the cathodic behavior of **1** under the same SEC conditions is affected by both the higher thermal reactivity of $1^{\bullet-}$ and the different steric properties of the 4,4'-dmbipy ligand. Despite appearing stable on the CV timescale (Figure 2(b)), the low temperature of 223 K set in the OTTLE cell was insufficient to completely stabilize the radical anion. IR monitoring of the electrolysis at R1 revealed simultaneous appearance of $1^{\bullet-}$ as the primary reduction product, and another dicarbonyl complex assigned as the PrCN-substituted 6-coordinate anion, $[1\text{-PrCN}]^-$ (Figure 13, Scheme 1) that replaces in the cooled

strongly coordinating solvent the $2e^-$ reduced 5-coordinate anion, $[1\text{-A}]^-$, in contrast to **3** and $[3\text{-A}]^-$. Radical anion $1^{\bullet-}$ is once again identified by the ca. 5 cm^{-1} high-energy shift of the $\nu(\text{CN})$ mode of coordinated NCS^- and the low-energy shift of the two $\nu(\text{CO})$ modes by some $20\text{-}30\text{ cm}^{-1}$, in this case from 1946 and 1862 cm^{-1} to 1922 and 1832 cm^{-1} . The presence of the singly reduced 4,4'-dmbipy ligand in $1^{\bullet-}$ has been confirmed by the parallel UV-vis monitoring of the reduction course (Figure E-S12, Supporting Information).

Table 2. IR and UV-vis absorption data for the complexes $[\text{Mo}(\eta^3\text{-allyl})(\text{CO})_2(x,x'\text{-dmbipy})(\text{NCS})]$, **1 ($x = 4$), and **3** ($x = 6$), and their reduction products (Scheme 1). See complete Table E-S4 (Supporting Information) including complex **2** ($x = 5$) and reference $[\text{Mo}(\eta^3\text{-allyl})(\text{CO})_2(\text{bipy})(\text{NCS})]$.**

Complex	$\nu(\text{CO})/\text{cm}^{-1}$	Calculated ^h $\nu(\text{CO})/\text{cm}^{-1}$	$\nu(\text{CN})/\text{cm}^{-1}$	Calculated ^h $\nu(\text{CN})/\text{cm}^{-1}$	$\lambda_{\text{max}}/\text{nm}$
$[\text{Mo}(\eta^3\text{-allyl})(\text{CO})_2(4,4'\text{-dmbipy})(\text{NCS})]$ ^a	1949, 1866	-	2080	-	470
$[\text{Mo}(\eta^3\text{-allyl})(\text{CO})_2(4,4'\text{-dmbipy})(\text{NCS})]$ ^{a,c}	1946, 1863	-	2084	-	-
$[\text{Mo}(\eta^3\text{-allyl})(\text{CO})_2(4,4'\text{-dmbipy})(\text{NCS})]$ ^b	1949, 1869	1882, 1800	2076	2056	-
$[\text{Mo}(\eta^3\text{-allyl})(\text{CO})_2(4,4'\text{-dmbipy})(\text{NCS})]$ ^{b,d}	1948, 1868	-	2078	-	-
$[\text{Mo}(\eta^3\text{-allyl})(\text{CO})_2(6,6'\text{-dmbipy})(\text{NCS})]$ ^a	1946, 1862	-	2078	-	470
$[\text{Mo}(\eta^3\text{-allyl})(\text{CO})_2(6,6'\text{-dmbipy})(\text{NCS})]$ ^{a,c}	1944, 1860	-	2082	-	-
$[\text{Mo}(\eta^3\text{-allyl})(\text{CO})_2(6,6'\text{-dmbipy})(\text{NCS})]$ ^b	1948, 1866	1881, 1800	2074	2054	-
$[\text{Mo}(\eta^3\text{-allyl})(\text{CO})_2(4,4'\text{-dmbipy})(\text{NCS})]^{\bullet-}$ ^{a,c}	1922, 1832	1855, 1763	2089	2070	388, 494, 538, > 600
$[\text{Mo}(\eta^3\text{-allyl})(\text{CO})_2(4,4'\text{-dmbipy})(\text{NCS})]^{\bullet-}$ ^{b,d}	1926, 1831	-	2084	-	-
$[\text{Mo}(\eta^3\text{-allyl})(\text{CO})_2(6,6'\text{-dmbipy})(\text{NCS})]^{\bullet-}$ ^{a,c}	1920, 1829	1855, 1764	2089	2069	396, 489, 518, > 600
$[\text{Mo}(\eta^3\text{-allyl})(\text{CO})_2(6,6'\text{-dmbipy})(\text{NCS})]^{\bullet-b}$	1925, 1834	-	2089	-	-
$[\text{Mo}(\eta^3\text{-allyl})(\text{CO})_2(6,6'\text{-dmbipy})(\text{NCS})]^{\bullet-a}$	1923, 1833	-	-	-	-
$[\text{Mo}(\eta^3\text{-allyl})(\text{CO})_2(4,4'\text{-dmbipy})(\text{PrCN})]^-$ ^{a,c}	1896, 1797	1797, 1705	2148 ⁱ	2229	350
$[\text{Mo}(\eta^3\text{-allyl})(\text{CO})_2(6,6'\text{-dmbipy})(\text{PrCN})]^-$ ^a	1904, 1789	1816, 1715	2148 ⁱ	2247	-
$[\text{Mo}(\eta^3\text{-allyl})(\text{CO})_2(4,4'\text{-dmbipy})]_2$ ^b	1891,1776, 1759	1775,1787, 1844,1858	-	-	-
$[\text{Mo}(\eta^3\text{-allyl})(\text{CO})_2(4,4'\text{-dmbipy})]^-$ ^{b,d}	1815, 1722	1741, 1656 ^e	-	-	-
$[\text{Mo}(\eta^3\text{-allyl})(\text{CO})_2(6,6'\text{-dmbipy})]^-$ ^{a,c}	1797, 1700 ^g	1803, 1702 ^f	-	-	420, 550
$[\text{Mo}(\eta^3\text{-allyl})(\text{CO})_2(6,6'\text{-dmbipy})]^-$ ^a	1807, 1700	-	-	-	-
$[\text{Mo}(\eta^3\text{-allyl})(\text{CO})_2(6,6'\text{-dmbipy})]^-$ ^b	1792, 1680 ⁱ	-	-	-	-

^a Measured in PrCN, ^b Measured in THF. ^c Measured at 223 K. ^d Measured at 268 K. ^e Calculated axial isomer. ^f Calculated equatorial isomer. ^g Broad absorption bands. ^h Some DFT data from Table DFT-S5 (Supporting Information) are reproduced here for clarity. ⁱ CN stretching mode of the PrCN ligand. ^j Values measured with an Au minigrad working electrode; the $\nu(\text{CO})$ values for a Pt minigrad are 1801 and 1717 cm^{-1} .

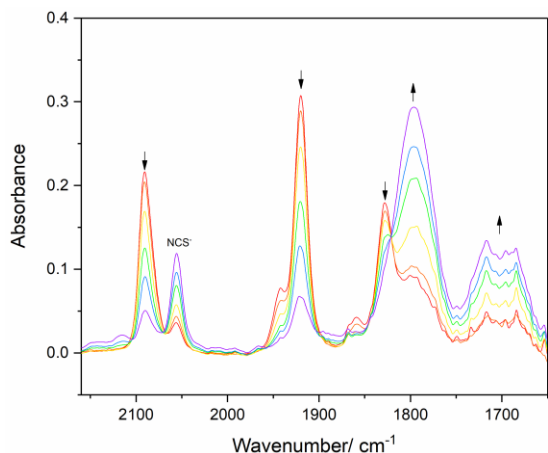


Figure 12. Controlled-potential IR SEC monitoring of the thermal conversion of $[\text{Mo}(\eta^3\text{-allyl})(\text{CO})_2(6,6'\text{-dmbipy})(\text{NCS})]^{-\bullet}$, $\mathbf{3}^{-\bullet}$ (\downarrow) to $[\mathbf{3-A}]^{-}$ (\uparrow) and free NCS^{-} between 223-293 K. Conditions: PrCN/TBAH, a cryostated OTTLE cell.

The new axial PrCN ligand in the second observed reduction product, $[\mathbf{1-PrCN}]^{-}$, is typically recognized in the IR spectrum by its low-intensity $\nu(\text{CN})$ absorption at 2147 cm^{-1} (Figure 13). The liberated NCS^{-} ligand absorbs again at 2050 cm^{-1} . The accompanying $\nu(\text{CO})$ bands at 1898 and 1797 cm^{-1} of $[\mathbf{1-PrCN}]^{-}$ are much narrower compared to those of 5-coordinate $[\mathbf{3-A}]^{-}$ (Figure 11(b)) and $[\mathbf{1-A}]^{-}$ formed in THF at 268 K (see below, Figure 14). A significant difference in $\nu(\text{CO})$ wavenumbers and band width was also encountered for related $2e^{-}$ reduced anions $[\text{Re}(\text{CO})_3(\text{bipy})]^{-}$ and $[\text{Re}(\text{CO})_3(\text{bipy})(\text{PrCN})]^{-}$.⁷⁸ The $\nu(\text{CO})$ wavenumbers do not correspond with any $1e^{-}$ reduced radical species, being much smaller than those of $\mathbf{1}^{-\bullet}$ (Table 2). On the other hand, they are much larger compared to $[\mathbf{1-A}]^{-}$ (Table 2) because the second added electron in the latter π -delocalized anion largely resides on the $\text{Mo}(\text{CO})_2$ moiety while in 6-coordinate $[\mathbf{1-PrCN}]^{-}$ on the (formally dianionic) bipy ligand (see the preceding DFT section). The UV-vis spectra corresponding to the IR SEC situation in Figure 13 also indicate the presence of two reduced species, one of which must be $\mathbf{1}^{-\bullet}$ absorbing at 388, 494, 538 and $>650\text{ nm}$. The electronic absorption arising around 350 nm is then assigned to $[\mathbf{1-PrCN}]^{-}$; importantly, the characteristic metallacycle $\pi\pi^*$ absorption of $[\mathbf{X-A}]^{-}$ at 500-600 nm (Table 2) is absent in this case (Figure E-S12, Supporting Information), in line with the IR SEC results. The comparison of the reduction paths of complexes $\mathbf{1}$ and $\mathbf{3}$ clearly reveals that the 6,6'-dmbipy ligands hinders coordination of PrCN to the Mo center of $[\mathbf{X-A}]^{-}$, probably not only for steric but also electronic reasons. Data in Table DFT-S5 (Supporting Information) testify that $[\mathbf{1-A}]^{-}$ prefers a different structure than $[\mathbf{3-A}]^{-}$, with an impact on the π -delocalization in the Mo-dmbipy metallacycle stabilizing the 5-coordinate geometry of the $2e^{-}$ reduced species.⁷⁹

Conducting the reduction of $\mathbf{1}$ in weakly coordinating THF at 268 K induces a very similar behavior as described above for $\mathbf{3}$ in the chilled PrCN electrolyte. In addition to intermediate $\mathbf{1}^{-\bullet}$, the main product formed at the cathodic wave R1 is now the 5-coordinate anion $[\mathbf{1-A}]^{-}$ absorbing in the $\nu(\text{CO})$ region at 1815 and 1722 cm^{-1} . The wavenumbers are much smaller compared to 6-coordinate $[\mathbf{1-PrCN}]^{-}$ (see above). On the other hand, both values are slightly larger than those determined for 5-coordinate $[\mathbf{1-A}]^{-}$ in chilled PrCN and in THF at ambient temperature (Table 2), while they should be smaller according the DFT calculations. This difference can be explained by the formation of a weak adduct of $[\mathbf{1-A}]^{-}$

with THF, causing slightly decreased electron density on the carbonyl ligands. Much larger $\nu(\text{CO})$ wavenumbers can be anticipated in this regard for ordinary 6-coordinate anion with coordinated THF, $[\mathbf{1-THF}]^{-}$.⁸⁰

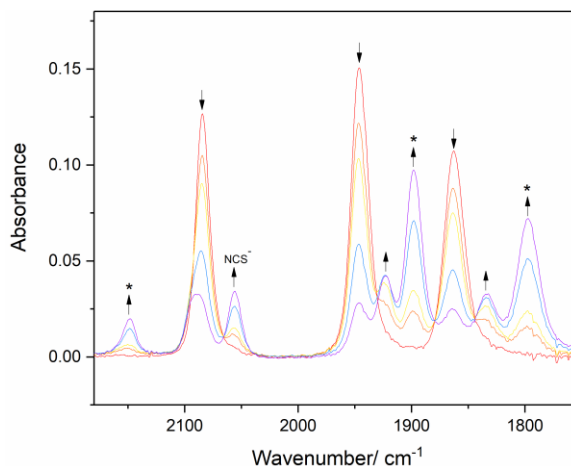


Figure 13. IR SEC monitoring of the electrochemical reduction of $[\text{Mo}(\eta^3\text{-allyl})(\text{CO})_2(4,4'\text{-dmbipy})(\text{NCS})]$, $\mathbf{1}$ (\downarrow) at the cathodic wave R1, forming $\mathbf{1}^{-\bullet}$ (\uparrow) and 6-coordinate $[\mathbf{1-PrCN}]^{-}$ (*). Conditions: PrCN/TBAH, 223 K, cryostated OTTLE cell.

The course of the reduction of $\mathbf{2}$ at R1 in PrCN at 223 K (Figure E-S13, Supporting Information) greatly combines features observed for $\mathbf{1}$ and $\mathbf{3}$, with the parallel production of radical anion $\mathbf{2}^{-\bullet}$ ($\nu(\text{CO})$ at $1921, 1831\text{ cm}^{-1}$), and 6-coordinate anion $[\mathbf{2-PrCN}]^{-}$ ($\nu(\text{CO})$ at $1897, 1789\text{ cm}^{-1}$) in a thermal equilibrium with five-coordinate anion $[\mathbf{2-A}]^{-}$ ($\nu(\text{CO})$ $1789, 1692\text{ cm}^{-1}$). This product representation was confirmed by the parallel UV-vis monitoring (Figure E-S14, Supporting Information). The visible region is dominated by the characteristically broad absorption of the 5-coordinate anion at around 600 nm. This experiment presents the most convincing evidence for the transition position of the 5,5'-dimethyl substitution at the redox active bipy ligands in the studied series.

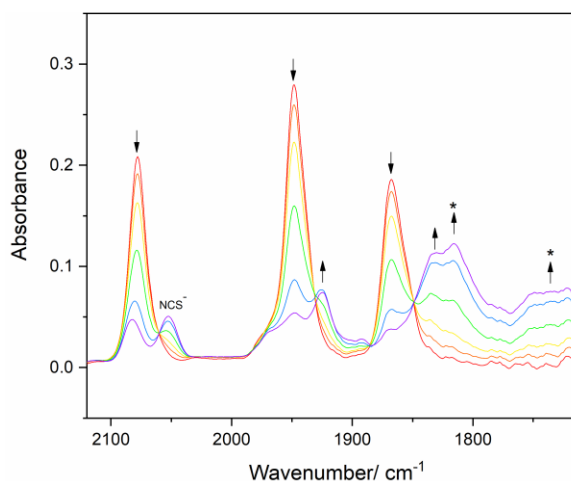


Figure 14. IR SEC monitoring of the reduction of $[\text{Mo}(\eta^3\text{-allyl})(\text{CO})_2(4,4'\text{-dmbipy})(\text{NCS})]$, $\mathbf{1}$ (\downarrow) at the cathodic wave R1,

generating $1^{\bullet-}$ (\uparrow) and five-coordinate $[1-A]^-$ ($*$) as a weak adduct with THF. Conditions: THF/TBAH, 268 K, cryostated OTTLE cell.

Infra-red spectroelectrochemistry at ambient temperature. The discussion of the generally more complicated cathodic paths and reactivity induced by the added electrons at room-temperature will be based on IR spectroelectrochemical results obtained in weakly coordinating THF and strongly coordinating PrCN. It focuses on participation of peculiar dimerization reactions of **1** and **2**, which are inhibited by cooling the electrolyte solution (see the preceding part).

It is convenient to start the description and discussion of the cathodic behavior at 293 K again with **3** bearing the sterically demanding 6,6'-dmbipy ligand. Notably, the reduction path in THF mirrors the temperature-controlled conversion of $1e^-$ reduced $3^{\bullet-}$ in PrCN at R1 to $2e^-$ reduced 5-coordinate $[3-A]^-$ via $[3-R]$ (Figure 12). Thus, during the reduction of **3** at R1, only a small amount of $3^{\bullet-}$ ($\nu(\text{CN})$: 2087 cm^{-1} , and $\nu(\text{CO})$: 1924, 1835 cm^{-1}) is initially detected (Figure 15), the transient species being readily converted to stable $2e^-$ reduced $[3-A]^-$ ($\nu(\text{CO})$: 1792, 1680 cm^{-1}). This process may involve an intermediate (a contact species) absorbing at 1900 cm^{-1} , differently from the instant low-temperature ECE path. It is worth mentioning that the wavenumbers of $[3-A]^-$ in this experiment are somewhat smaller than those measured in PrCN at 223 K (Table 2). This observation indicates a weak interaction between $[3-A]^-$ and PrCN at the low temperature. The spectral variability in the $\nu(\text{CO})$ region is thus a common feature in the whole series of $[X-A]^-$.

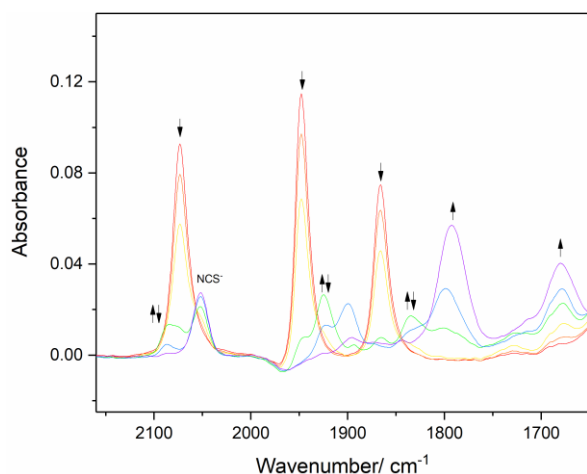


Figure 15. IR SEC monitoring of the initial reduction of $[\text{Mo}(\eta^3\text{-allyl})(\text{CO})_2(6,6'\text{-dmbipy})(\text{NCS})]$, **3** (\downarrow) at R1 to 5-coordinate $[3-A]^-$ (\uparrow) via intermediate $3^{\bullet-}$ ($\uparrow\downarrow$). Conditions: THF/TBAH, 293 K, OTTLE cell.

The cathodic path of **3** leading to $[3-A]^-$ in PrCN at 293 K (Figure E-S15, Supporting Information) is less straightforward than in THF. The initially detectable reduced species shows two $\nu(\text{CO})$ bands at 1923 and 1797 cm^{-1} , being accompanied by free thiocyanate absorbing at 1950 cm^{-1} . The absence of the $\nu(\text{CN})$ absorption of the coordinated thiocyanate (typically above the parent absorption at 2074 cm^{-1}) excludes the formation of $3^{\bullet-}$. The higher stability of the reduced dicarbonyl complex formed,

compared to $3^{\bullet-}$ in THF (Figure 15), supports its tentative assignment as the solvento radical $[\text{Mo}(\eta^3\text{-allyl})(\text{CO})_2(6,6'\text{-dmbipy})(\text{PrCN})]$, $[3\text{-PrCN}]$. As anticipated, the concomitant reduction of this complex produces $[3\text{-PrCN}]^-$ ($\nu(\text{CO})$ at 1904 and 1789 cm^{-1}) that was not detected along the straightforward ECE route at 223 K (Figure 12). It is therefore not surprising that the $2e^-$ reduced 6-coordinate anion is unstable also at 293 K and converts gradually to 5-coordinate $[3-A]^-$ ($\nu(\text{CO})$ at 1807 and 1700 cm^{-1}). The described peculiar cathodic path also includes a contact species ($\nu(\text{CO})$ absorption at 1832 and 1733 cm^{-1}), arising from the co-existence of $[3\text{-PrCN}]$ and $[3-A]^-$. This absorbance disappears during the follow-up reduction of $[3\text{-PrCN}]$ to $[3\text{-PrCN}]^-$, the latter converting ultimately to genuine $[3-A]^-$. The main factor responsible for the different reduction paths of **3** in PrCN at 223 and 293K, and in THF at 293 K, is the (in)stability of $3^{\bullet-}$ as the primary $1e^-$ reduction product. It is also noteworthy that the $\nu(\text{CO})$ wavenumbers of $[3\text{-PrCN}]$ (1923, 1797 cm^{-1}) are very similar to those calculated (using the scaling factor of 0.97) for the equatorial isomer of 5-coordinate radical $[3-R]$ (Table DFT-S5, Supporting Information). This means that differently from THF, where $[3-R]$ is directly reducible to $[3-A]^-$, the 5-coordinate radical becomes stabilized by a weak bonding interaction with PrCN. There is no evidence for its secondary dimerization (Scheme 1), pointing to the protective role of the 6,6'-dmbipy ligand.

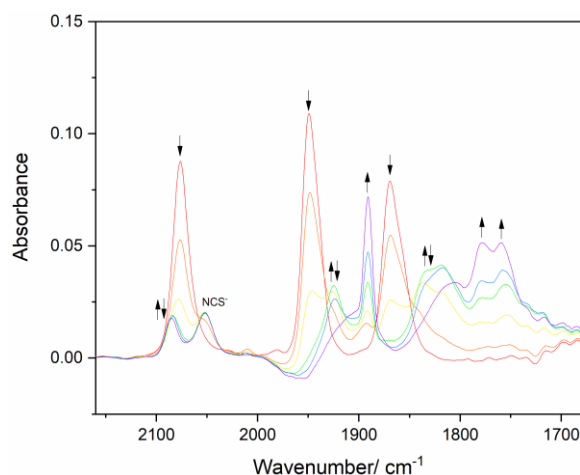


Figure 16. IR SEC monitoring of the $1e^-$ reduction of $[\text{Mo}(\eta^3\text{-allyl})(\text{CO})_2(4,4'\text{-dmbipy})(\text{NCS})]$, **1** (\downarrow) at R1 to intermediate $1^{\bullet-}$ ($\downarrow\uparrow$) concomitantly converting to $[\text{Mo}(\eta^3\text{-allyl})(\text{CO})_2(4,4'\text{-dmbipy})]_2$ -related dimer $[1-D]$ (\uparrow). Conditions: THF/TBAH, 293 K, OTTLE cell.

Reducing **1** in THF at 293 K, already the first cathodic step at the electrode potential of R1 shows a striking difference from the reduction of **3** that converts under the same conditions of thin-layer electrolysis exclusively to 5-coordinate anion $[3-A]^-$ (typically broad $\nu(\text{CO})$ bands at 1792, 1680 cm^{-1}). For **1**, the corresponding anionic species, $[1-A]^-$, was only detected at 268 K as a weak adduct with THF (Table 2). At room temperature, instead, no $[1-A]^-$ was formed at R1 and the dominant product (apart from minor $1^{\bullet-}$ still detectable in the thin-solution layer of the OTTLE cell) showed an unprecedented IR spectral pattern of three narrow $\nu(\text{CO})$ bands at 1891, 1778 and 1759 cm^{-1} (Figure 16). These values of absorption maxima reasonably agree with the $\nu(\text{CO})$ wavenumbers obtained with DFT for the staggered structure of the Mo–Mo bound dimer $[\text{Mo}(\eta^3\text{-allyl})(\text{CO})_2(4,4'\text{-dmbipy})]_2$, $[1-D]$ (Figure 9, and Tables DFT-S5 and E-S4, Supporting Information). The calculated intensity pattern of the

four $\nu(\text{CO})$ modes for [1-D], 1858 (medium), 1844 (strong), 1787 (strong), and 1775 (weak), has been encountered⁸¹ for the tetracarbonyl dimer $[\text{Ru}(\text{CO})_2(\text{iPr-DAB})(\text{Me})]_2$ (iPr-DAB = 1,4-diisopropyl-1,4-diaza-buta-1,3-diene). For **1**, the exact molecular structure of the dimeric end-product showing the different $\nu(\text{CO})$ intensity pattern (1-D'), is unknown at present. However, it is assumed to be closely related to the metal-metal bound dimers represented by $[\text{Ru}(\text{CO})_2(\text{iPr-DAB})(\text{Me})]_2$ and $[\text{Mn}(\text{CO})_3(\text{bipy})]_2$, resulting from the general ECEC cathodic route shown also in Scheme 1, which has been based on the evidence gained from faster cyclic voltammetry. A strong argument for a different, reinforced structure of [1-D'] is its subsequent reduction that does not convert it to 5-coordinate anion, [1-A]⁻, which is a typical ECE step for both Ru-Ru and Mn-Mn dimers, but most likely to singly reduced [1-D']⁻. For $[\text{Mo}(\eta^3\text{-allyl})(\text{CO})_2(\text{bipy})(\text{NCS})]$, with a cathodic behavior closest to that of **1**, the equivalent of [1-D'] absorbs in the IR CO-stretching region at 1891, 1778 and 1757 cm^{-1} .⁴⁵ The subsequent reduction shifts this assembly down to 1844, 1723 and 1700(sh) cm^{-1} . The latter wavenumbers were assigned incorrectly to $[\text{Mo}(\eta^3\text{-allyl})(\text{CO})_2(\text{bipy})]^-$, which is actually hardly seen in THF at 293 K, similar to [1-A]⁻. It remains a challenge to prepare, isolate and characterize [1-D'] in a follow-up study.

Reducing **1** at room temperature in PrCN (Figure E-S16, Supporting Information), dimer [1-D] is again the dominant product, suggesting that under ambient conditions there is a strong driving force to form this species. The intimate mechanism is slightly different from that in THF, with [1-PrCN], and [1-A]⁻ in a weak contact with PrCN, being involved as intermediate species.

Much like at low temperature in PrCN (see above), reduction of **2** in THF at 293 K (Figure E-S17) represents an intermediate case between the routes of **1** and **3**, producing ultimately a mixture of both the 5-coordinate anion and a dimer. The $[\text{Mo}(\eta^3\text{-allyl})(\text{CO})_2(5,5'\text{-dmbipy})]_2$ -related dimer, [2-D'], is revealed by the three $\nu(\text{CO})$ bands at 1892 (sharp), 1780 and 1761 cm^{-1} ; the $\nu(\text{CO})$ wavenumbers of $[\text{Mo}(\eta^3\text{-allyl})(\text{CO})_2(5,5'\text{-dmbipy})]^-$ (1820, 1730 cm^{-1}) point to its weak interaction with THF. A very similar cathodic path is followed by **2** in PrCN (Figure E-S18).

Cyclic Voltammetry and IR Spectroelectrochemistry under a CO₂ atmosphere. The CV study of **1** and **3** was repeated in CO₂-saturated weakly coordinating THF at both Pt and Au cathodes, to probe the catalytic activity of the complexes towards CO₂ reduction and identify the catalyst. For both complexes the initial cathodic wave R1 (Table 1 and Tables E-S1 and E-S2, Supporting Information) remains unchanged, excluding any thermal reaction or adsorption effects. Inspecting the CV of **1** at an Au cathode in CO₂-saturated THF (Figure 17), the reduction at R1 does not produce any detectable 5-coordinate anions [1-A]⁻ that would be reoxidized (under Ar) at the anodic wave O1' (Figure 2). The adduct of the anion with CO₂, [1-CO₂]⁻, has been calculated (Figure 10) and analyzed with DFT. Some catalytic current enhancement is not seen already at R1 but at a more negative potential close to the reduction of dimer [1-D] at R(D). This observation indicates that either further reduction of [1-CO₂]⁻ or its transformation product at a potential close to R(D) is needed to trigger the catalytic process, or that the dimerization seen for [1-CO₂]⁻ in THF under argon cannot be inhibited under CO₂ and the concomitant dimer reduction is

needed to regenerate catalyst [1-CO₂]⁻. The first route resembles tricarbonyl Mn-iPr-DAB (iPr-DAB = 1,4-diisopropyl-1,4-diaza-buta-1,3-diene) complexes forming 2e⁻ reduced 5-coordinate anions via an ECE mechanism, which react with CO₂ to form a Mn-bicarbonate intermediate reducible some 600 mV more negatively than the parent complex, to restore the catalytic activity.⁸² IR monitoring of the electrolysis at R1 was needed to collect a supporting evidence for either pathway, see below.

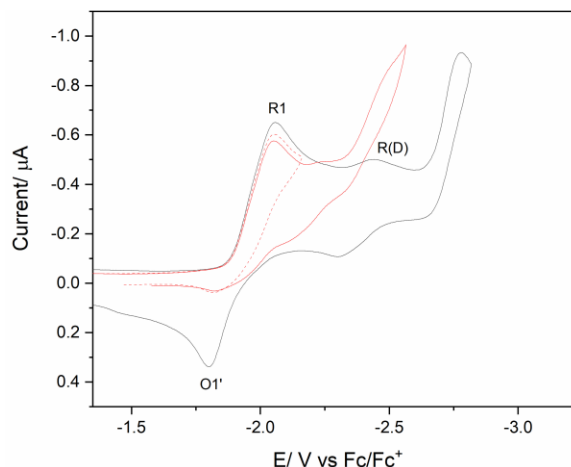


Figure 17. Cyclic voltammetry of $[\text{Mo}(\eta^3\text{-allyl})(\text{CO})_2(4,4'\text{-dmbipy})(\text{NCS})]$ (**1**) in CO₂-saturated (red) or Ar-saturated (black) THF/TBAH at an Au microdisc electrode. Scan rate: 100 mV s^{-1} .

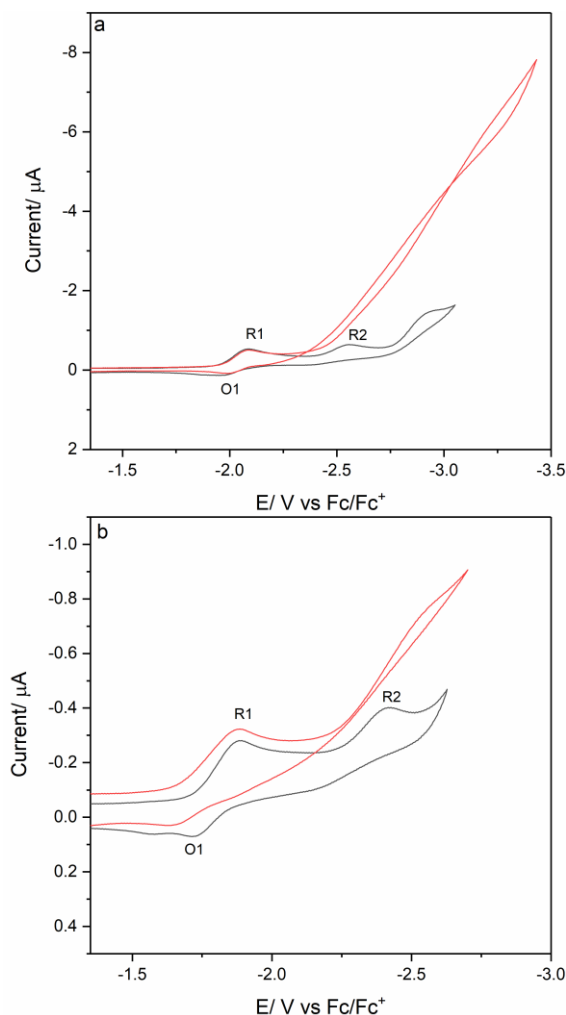


Figure 18. Cyclic voltammetry of $[\text{Mo}(\eta^3\text{-allyl})(\text{CO})_2(6,6'\text{-dmbipy})(\text{NCS})]$ (**3**) in CO_2 -saturated (red) and Ar-saturated (black) THF/TBAH at Au microdisc (a) and Pt microdisc (b) electrodes. Scan rate: 100 mV s^{-1} .

The cathodic behavior of **3** in THF in the presence of excess CO_2 on the short time scale of cyclic voltammetry is straightforward, given the relative stability of singly reduced radical anions $[\mathbf{3}]^{\cdot-}$ formed at R1 and further reducible to $[\mathbf{3-A}]^-$ at R2 (Figure 18). Similar to $[\mathbf{1-A}]^-$, also $[\mathbf{3-A}]^-$ reacts with CO_2 to form initially $[\mathbf{3-CO}_2]^-$, triggering the catalytic CO_2 reduction at R2. The higher catalytic current on Au (Figure 18a) compared to Pt (Figure 18b) indicates an involvement of the cathodic surface in the catalytic process. The increased catalytic efficiency may result from a strong stabilizing interaction between the gold surface and $[\mathbf{3-A}]^-$ which has recently been proven for the $[\text{Mo}(\text{CO})_4(\text{bipy})]$ family of catalysts.⁴² Compared to $[\text{Mo}(\eta^3\text{-allyl})(\text{CO})_2(\text{bipy})(\text{NCS})]$,⁴³ the anionic catalyst derived from **3** operates with higher efficiency – with a higher catalytic current flowing at a lower overpotential. This difference can be ascribed to a higher stability of $[\mathbf{3-A}]^-$, as $[\text{Mo}(\eta^3\text{-allyl})(\text{CO})_2(\text{bipy})]^-$ was hardly detectable by in situ IR spectroscopy. In this case, IR spectroelectrochemistry of **3** on the time scale of minutes was expected to provide an evidence for the catalytic activity of $[\mathbf{3-A}]^-$ towards CO_2 already at the cathodic wave R1 (in line with Figure 15).

The reduction of **1** at R1 in CO_2 -saturated THF monitored by infrared spectroscopy led to a mixture of detectable products.

The $\nu(\text{CO})$ absorption at 1893 and 1760 cm^{-1} almost certainly belongs to dimer $[\mathbf{1-D}']$ (Figure 16), which supports the dimerization process seen with cyclic voltammetry (Figure 17). As expected, there is no 5-coordinate $[\mathbf{1-A}]^-$ observed in the IR spectra at room temperature (Figure 14). However, compared to Figure 16, representing the cathodic route of **1** in THF under argon, the $\nu(\text{CO})$ absorptions at 1910 and 1802 cm^{-1} , seen in Figure E-S19 (Supporting Information), are not much different from the wavenumbers predicted for the 6-coordinate anion $[\mathbf{1-CO}_2]^-$ (1905 , 1780 cm^{-1}), using the difference between the $\nu(\text{CO})$ values measured and calculated for $[\mathbf{1-A}]^-$ (Table 2, 90 and 58 cm^{-1}), and the $\nu(\text{CO})$ values calculated for $[\mathbf{1-CO}_2]^-$. Another reasoning, based on comparison of $\nu(\text{CO})$ measured and calculated for $[\mathbf{1}]^{\cdot-}$ (Table 2) and measured for some bonding interaction between $[\mathbf{1-A}]^-$ and measured for $[\mathbf{1-CO}_2]^-$ (see above) predicts the values calculated for $[\mathbf{1-CO}_2]^-$ to be 1839 and 1735 cm^{-1} , which are reasonably close to the values of 1831 and 1714 cm^{-1} calculated for the DFT-optimized structure of $[\mathbf{1-CO}_2]^-$ depicted in Figure 10. The interaction between $[\mathbf{1-A}]^-$ and CO_2 has also been revealed by conventional cyclic voltammetry (Figure 17). In Figure ES-19 (Supporting Information), there is a concurrent appearance of small bands at 1674 and 1641 cm^{-1} indicating the formation of free bicarbonate anion (and, indirectly, CO). At the same time, a small amount of free formate (1600 cm^{-1}) starts to appear from the very beginning of the thin-layer electrolysis of **1** at R1. The limited reductive conversion of dissolved CO_2 , testified by only a small decrease in the intensity of the satellite $^{13}\text{CO}_2$ peak, is in agreement with the relative stability of $[\mathbf{1-CO}_2]^-$ under the aprotic conditions. The formation of $[\mathbf{1-D}']$ can also be considered as an inhibiting factor.

In argon-saturated THF at 293 K , **3** forms at R1 $2e^-$ reduced $[\mathbf{3-A}]^-$ with the smallest IR $\nu(\text{CO})$ wavenumbers of 1792 and 1680 cm^{-1} indicating the absence of any interaction with the weak donor solvent (Figure 15). The presence of CO_2 in the THF electrolyte has some impact on the $\nu(\text{CO})$ wavenumbers of the five-coordinate anion, which slightly increase to $1801/1792$ and $1697/1673 \text{ cm}^{-1}$ (Figure E-S20(a), Supporting Information). The behavior does not correspond with the formation of $[\mathbf{3-CO}_2]^-$ seen above for **1** with a less hindered Mo-dmbipy metallacycle. Rather, $[\mathbf{3-CO}_2]^-$ interacts only weakly with CO_2 , similar to PrCN at variable temperature (Figures 11 and 12). Moving the cathodic potential from R1 more negatively, towards R2 (in the ordinary CV of **3**), results in IR spectral changes (Figure E-S20(b), Supporting Information) revealing some catalytic conversion of CO_2 to free formate and CO (flanked by the characteristic absorption of the bicarbonate anion). The $\nu(\text{CO})$ absorption of $[\mathbf{3-CO}_2]^-$ becomes diminished while there is a continuous growth of $\nu(\text{CO})$ absorption labelled by asterisk in Figure E-S20(b) (Supporting Information), which most likely corresponds to the inactive dimer, $[\mathbf{3-D}']$, seen also for **1**, representing a deactivation route.

CONCLUSIONS

The position of the methyl substituents in the studied series of x,x' -dmbipy ($x = 4-6$) complexes plays a key role in determining the cathodic paths at variable temperature. There is a direct linear relationship between the position of the methyl group and the stability of both the $1e^-$ reduced primary radical anion and $2e^-$ reduced 5-coordinate anionic complex increasing in the direction of $x = 4 < 5 < 6$. This trend reflects an interplay of both steric (dmbipy planarity, Mo–NCS packing) and electronic (Mo–NCS bond strength, delocalized π -bonding) factors. At the ca-

thodic wave R1, the reduction of **1** produces the unstable radical anions and the five-coordinate anions. The latter product converts to an unreactive dimer that may also exist in its reduced form; the molecular structure of the end-product, seen in both THF and PrCN, remains to be elucidated. This behavior excludes an unsupported Mo–Mo bond between 5-coordinate radical units. Radical anions derived from **3** are most stable, surprisingly more than the congeners with unsubstituted bipy as a weaker donor ligand; at ambient temperature they transform exclusively to the 5-coordinate anions (in a CE step) that hardly bind donor solvents or dimerize. The key differences in the cathodic paths of **1** and **3**, in particular the different coordinating ability of $2e^-$ reduced $[X-A]^-$, persist also in the presence of CO_2 dissolved in the thin solution layer of the electrolyte. Further differences and enhanced catalytic activity can be expected upon the addition of Brønsted or Lewis acids, to complete the comparative study stimulated by the development in the field of the electrocatalytic CO_2 reduction with $[Mn(CO)_3(R-bipy)X]$. Variation of the α -diimine nature and backbone substitution, as well as probing substituents on the allyl ligand, are a few possible routes that warrant attention to continue the investigation of the peculiar redox behavior, reactivity and catalytic activity of this challenging yet largely unexplored family of organometallic compounds.

ASSOCIATED CONTENT

Supporting Information

The following three sections with independent numbering of Tables and Figures.

Crystallographic_data (PDF)

Supplementary_electrochemical_data (PDF)

Supplementary_DFT data (PDF)

AUTHOR INFORMATION

Corresponding Author

E-mail: f.hartl@reading.ac.uk

ORCID

F. Hartl: 0000-0002-7013-5360

M. J. Calhorda: 0000-0002-6872-3569

A. M. Chippindale: 0000-0002-5918-8701

Notes

The authors declare no competing financial interest.

ACKNOWLEDGEMENTS

This work was jointly funded by the EPSRC and Spectroelectrochemistry Reading (a spin-out company of the University of Reading – F.H.). F.L.P.V. thanks Erasmus+ (EU) for her Traineeship. The University of Reading is acknowledged for the provision of the Chemical Analysis Facility (the CAF lab) – NMR and X-ray diffraction analyses. Mr Nick Spencer (University of Reading) is thanked for his help in collecting the single-crystal X-ray diffraction data. M.J.C. thanks the Fundação para a Ciência e a Tecnologia, Portugal, for financial support (UID/MULTI/00612/2013) and the grant SFRH/BSAB/135473/2017.

REFERENCES

- (1) Monthly Average Mauna Loa CO_2 <https://www.esrl.noaa.gov/gmd/ccgg/trends/index.html> (accessed Jul 21, 2018).
- (2) Centi, G.; Perathoner, S. Opportunities and Prospects in the Chemical Recycling of Carbon Dioxide to Fuels. *Catal. Today* **2009**, *148*, 191–205.
- (3) *Electrochemical Reduction of Carbon Dioxide - Overcoming the Limitations of Photosynthesis*; Marken, F., Fermin, D., Eds.; Energy and Environment Series; Royal Society of Chemistry: Cambridge, 2018.
- (4) Qiao, J.; Liu, Y.; Hong, F.; Zhang, J. A Review of Catalysts for the Electroreduction of Carbon Dioxide to Produce Low-Carbon Fuels. *Chem. Soc. Rev.* **2014**, *43*, 631–675.
- (5) Angamuthu, R.; Byers, P.; Lutz, M.; Spek, A. L.; Bouwman, E. Electrocatalytic CO_2 Conversion to Oxalate by a Copper Complex. *Science* **2010**, *327*, 313–315.
- (6) Windle, C. D.; Perutz, R. N. Advances in Molecular Photocatalytic and Electrocatalytic CO_2 Reduction. *Coord. Chem. Rev.* **2012**, *256*, 2562–2570.
- (7) Hawecker, J.; Lehn, J.-M.; Ziesel, R. Electrocatalytic Reduction of Carbon Dioxide Mediated by $Re(Bipy)(CO)_3Cl$ (Bipy = 2,2'-Bipyridine). *J. Chem. Soc. Chem. Commun.* **1984**, *984*, 328.
- (8) Machan, C. W.; Chabolla, S. A.; Yin, J.; Gilson, M. K.; Tezcan, F. A.; Kubiak, C. P. Supramolecular Assembly Promotes the Electrocatalytic Reduction of Carbon Dioxide by $Re(I)$ Bipyridine Catalysts at a Lower Overpotential. *J. Am. Chem. Soc.* **2014**, *136*, 14598–14607.
- (9) Ching, H. Y. V.; Wang, X.; He, M.; Perujo Holland, N.; Guillot, R.; Slim, C.; Griveau, S.; Bertrand, H. C.; Policar, C.; Bedioui, F.; et al. Rhenium Complexes Based on 2-Pyridyl-1,2,3-Triazole Ligands: A New Class of CO_2 Reduction Catalysts. *Inorg. Chem.* **2017**, *56*, 2966–2976.
- (10) Wilting, A.; Stolper, T.; Mata, R. A.; Siewert, I. Dinuclear Rhenium Complex with a Proton Responsive Ligand as a Redox Catalyst for the Electrochemical CO_2 Reduction. *Inorg. Chem.* **2017**, *56*, 4176–4185.
- (11) Stanton, C. J.; Machan, C. W.; Vandezande, J. E.; Jin, T.; Majetich, G. F.; Schaefer, H. F.; Kubiak, C. P.; Li, G.; Agarwal, J. $Re(I)$ NHC Complexes for Electrocatalytic Conversion of CO_2 . *Inorg. Chem.* **2016**, *55*, 3136–3144.
- (12) Maurin, A.; Ng, C.-O.; Chen, L.; Lau, T.-C.; Robert, M.; Ko, C.-C. Photochemical and Electrochemical Catalytic Reduction of CO_2 with NHC-Containing Dicarbonyl Rhenium(I) Bipyridine Complexes. *Dalton Trans.* **2016**, *45*, 14524–14529.
- (13) Hadadzadeh, H.; Farrokhpour, H.; Simpson, J.; Shakeri, J.; Daryanavard, M.; Shokrollahi, M. Electrocatalytic Reduction of CO_2 to CO by a Mononuclear Ruthenium(II) Complex. *New J. Chem.* **2016**, *40*, 6347–6357.
- (14) Chen, Z.; Chen, C.; Weinberg, D. R.; Kang, P.; Concepcion, J. J.; Harrison, D. P.; Brookhart, M. S.; Meyer, T. J. Electrocatalytic Reduction of CO_2 to CO by Polypyridyl Ruthenium Complexes. *Chem. Commun.* **2011**, *47*, 12607–12609.
- (15) Daryanavard, M.; Hadadzadeh, H.; Weil, M.; Farrokhpour, H. Electrocatalytic Reduction of CO_2 to CO in the Presence of a Mononuclear Polypyridyl Ruthenium(II) Complex. *J. CO₂ Util.* **2017**, *17*, 80–89.

- (16) Szymaszek, A.; Pruchnik, F. P. Electrochemical Reduction of Carbon Dioxide in the Presence of $\text{RhCl}(\text{CO})(\text{PPh}_3)_2$ and $\text{IrCl}(\text{CO})(\text{PPh}_3)_2$. *J. Organomet. Chem.* **1989**, *376*, 133–140.
- (17) Ahn, S. T.; Bielinski, E. A.; Lane, E. M.; Chen, Y.; Bernskoetter, W. H.; Hazari, N.; Palmore, G. T. R. Enhanced CO_2 Electroreduction Efficiency through Secondary Coordination Effects on a Pincer Iridium Catalyst. *Chem. Commun.* **2015**, *51*, 5947–5950.
- (18) Sypaseuth, F. D.; Matlachowski, C.; Weber, M.; Schwalbe, M.; Tzschucke, C. C. Electrocatalytic Carbon Dioxide Reduction by Using Cationic Pentamethylcyclopentadienyl-Iridium Complexes with Unsymmetrically Substituted Bipyridine Ligands. *Chem. Eur. J.* **2015**, *21*, 6564–6571.
- (19) Roy, S.; Sharma, B.; Pécaut, J.; Simon, P.; Fontecave, M.; Tran, P. D.; Derat, E.; Artero, V. Molecular Cobalt Complexes with Pendant Amines for Selective Electrocatalytic Reduction of Carbon Dioxide to Formic Acid. *J. Am. Chem. Soc.* **2017**, *139*, 3685–3696.
- (20) Neri, G.; Walsh, J. J.; Wilson, C.; Reynal, A.; Lim, J. Y. C.; Li, X.; White, A. J. P.; Long, N. J.; Durrant, J. R.; Cowan, A. J. A Functionalised Nickel Cyclam Catalyst for CO_2 reduction: Electrocatalysis, Semiconductor Surface Immobilisation and Light-Driven Electron Transfer. *Phys. Chem. Chem. Phys.* **2015**, *17*, 1562–1566.
- (21) Song, J.; Klein, E. L.; Neese, F.; Ye, S. The Mechanism of Homogeneous CO_2 reduction by $\text{Ni}(\text{Cyclam})$: Product Selectivity, Concerted Proton-Electron Transfer and C-O Bond Cleavage. *Inorg. Chem.* **2014**, *53*, 7500–7507.
- (22) Bourrez, M.; Molton, F.; Chardon-Noblat, S.; Deronzier, A. $[\text{Mn}(\text{Bipyridyl})(\text{CO})_3\text{Br}]$: An Abundant Metal Carbonyl Complex as Efficient Electrocatalyst for CO_2 Reduction. *Angew. Chemie Int. Ed.* **2011**, *50*, 9903–9906.
- (23) Spall, S. J. P.; Keane, T.; Tory, J.; Cocker, D. C.; Adams, H.; Fowler, H.; Meijer, A. J. H. M.; Hartl, F.; Weinstein, J. A. Manganese Tricarbonyl Complexes with Asymmetric 2-Iminopyridine Ligands: Toward Decoupling Steric and Electronic Factors in Electrocatalytic CO_2 Reduction. *Inorg. Chem.* **2016**, *55*, 12568–12582.
- (24) Sampson, M. D.; Kubiak, C. P. Manganese Electrocatalysts with Bulky Bipyridine Ligands: Utilizing Lewis Acids To Promote Carbon Dioxide Reduction at Low Overpotentials. *J. Am. Chem. Soc.* **2016**, *138*, 1386–1393.
- (25) Sampson, M. D.; Nguyen, A. D.; Grice, K. a.; Moore, C. E.; Rheingold, A. L.; Kubiak, C. P. Manganese Catalysts with Bulky Bipyridine Ligands for the Electrocatalytic Reduction of Carbon Dioxide: Eliminating Dimerization and Altering Catalysis. *J. Am. Chem. Soc.* **2014**, *136*, 5460–5471.
- (26) Smieja, J. M.; Sampson, M. D.; Grice, K. A.; Benson, E. E.; Froehlich, J. D.; Kubiak, C. P. Manganese as a Substitute for Rhenium in CO_2 Reduction Catalysts: The Importance of Acids. *Inorg. Chem.* **2013**, *52*, 2484–2491.
- (27) Franco, F.; Cometto, C.; Nencini, L.; Barolo, C.; Sordello, F.; Minero, C.; Fiedler, J.; Robert, M.; Gobetto, R.; Nervi, C. Local Proton Source in Electrocatalytic CO_2 Reduction with $[\text{Mn}(\text{Bpy-R})(\text{CO})_3\text{Br}]$ Complexes. *Chem. Eur. J.* **2017**, *23*, 4782–4793.
- (28) Grills, D. C.; Ertem, M. Z.; McKinnon, M.; Ngo, K. T.; Rochford, J. Mechanistic Aspects of CO_2 Reduction Catalysis with Manganese-Based Molecular Catalysts. *Coord. Chem. Rev.* **2018**, *374*, 173–217.
- (29) Azcarate, I.; Costentin, C.; Robert, M.; Savéant, J. M. Through-Space Charge Interaction Substituent Effects in Molecular Catalysis Leading to the Design of the Most Efficient Catalyst of CO_2 -to- CO Electrochemical Conversion. *J. Am. Chem. Soc.* **2016**, *138*, 16639–16644.
- (30) Costentin, C.; Robert, M.; Savéant, J. M. Current Issues in Molecular Catalysis Illustrated by Iron Porphyrins as Catalysts of the CO_2 -to- CO Electrochemical Conversion. *Acc. Chem. Res.* **2015**, *48*, 2996–3006.
- (31) Mohamed, E. A.; Zahran, Z. N.; Naruta, Y. Efficient Electrocatalytic CO_2 Reduction with a Molecular Cofacial Iron Porphyrin Dimer. *Chem. Commun.* **2015**, *51*, 16900–16903.
- (32) Elgrishi, N.; Chambers, M. B.; Wang, X.; Fontecave, M. Molecular Polypyridine-Based Metal Complexes as Catalysts for the Reduction of CO_2 . *Chem. Soc. Rev.* **2017**, *46*, 761–796.
- (33) Francke, R.; Schille, B.; Roemelt, M. Homogeneously Catalyzed Electroreduction of Carbon Dioxide - Methods, Mechanisms, and Catalysts. *Chem. Rev.* **2018**, *118*, 4631–4701.
- (34) Grice, K. A. Carbon Dioxide Reduction with Homogenous Early Transition Metal Complexes: Opportunities and Challenges for Developing CO_2 Catalysis. *Coord. Chem. Rev.* **2017**, *336*, 78–95.
- (35) Grice, K. A.; Saucedo, C. Electrocatalytic Reduction of CO_2 by Group 6 $\text{M}(\text{CO})_6$ Species without “Non-Innocent” Ligands. *Inorg. Chem.* **2016**, *55*, 6240–6246.
- (36) Clark, M. L.; Grice, K. A.; Moore, C. E.; Rheingold, A. L.; Kubiak, C. P. Electrocatalytic CO Reduction by $\text{M}(\text{Bpy-R})(\text{CO})_4$ ($\text{M} = \text{Mo}, \text{W}$; $\text{R} = \text{H}, \text{tBu}$) Complexes. Electrochemical, Spectroscopic, and Computational Studies and Comparison with Group 7 Catalysts. *Chem. Sci.* **2014**, *5*, 1894–1900.
- (37) Tory, J.; Setterfield-Price, B.; Dryfe, R. A. W.; Hartl, F. $[\text{M}(\text{CO})_4(2,2'\text{-Bipyridine})]$ ($\text{M} = \text{Cr}, \text{Mo}, \text{W}$) Complexes as Efficient Catalysts for Electrochemical Reduction of CO_2 at a Gold Electrode. *ChemElectroChem* **2015**, *2*, 213–217.
- (38) Franco, F.; Cometto, C.; Sordello, F.; Minero, C.; Nencini, L.; Fiedler, J.; Gobetto, R.; Nervi, C. Electrochemical Reduction of CO_2 by $\text{M}(\text{CO})_4(\text{Diimine})$ Complexes ($\text{M} = \text{Mo}, \text{W}$): Catalytic Activity Improved by 2,2'-Dipyridylamine. *ChemElectroChem* **2015**, *2*, 1372–1379.
- (39) Hartl, F.; Taylor, J. O.; Leavey, R. D. Solvent and Ligand Substitution Effects on Electrocatalytic Reduction of CO_2 with $[\text{Mo}(\text{CO})_4(x,x'\text{-dimethyl-}2,2'\text{-bipyridine})]$ ($x = 4\text{-}6$) Enhanced at a Gold Cathodic Surface. *ChemElectroChem*. DOI: 10.1002/celec.201800879
- (40) Sieh, D.; Lacy, D. C.; Peters, J. C.; Kubiak, C. P. Reduction of CO_2 by Pyridine Monoimine Molybdenum Carbonyl Complexes: Cooperative Metal-Ligand Binding of CO_2 . *Chem. Eur. J.* **2015**, *21*, 8497–8503.
- (41) Ngo, K. T.; McKinnon, M.; Mahanti, B.; Narayanan, R.; Grills, D. C.; Ertem, M. Z.; Rochford, J. Turning on the Protonation-First Pathway for Electrocatalytic CO_2 Reduction by Manganese Bipyridyl Tricarbonyl Complexes. *J. Am. Chem. Soc.* **2017**, *139*, 2604–2618.
- (42) a) Neri, G.; Donaldson, P. M.; Cowan, A. J. The Role of Electrode-Catalyst Interactions in Enabling Efficient CO_2 Reduction with $\text{Mo}(\text{Bpy})(\text{CO})_4$ As Revealed by Vibrational Sum-Frequency Generation Spectroscopy. *J. Am. Chem. Soc.* **2017**, *139*, 13791–13797. b) Neri, G.; Teobaldi, G.; Walsh, J. J.; Donaldson, P. M. & Cowan A. J. Detection of catalytic intermediates at an electrode surface during carbon dioxide reduction by an earth-abundant catalyst. *Nat. Catal.* Accepted.

- (43) Rotundo, L.; Garino, C.; Gobetto, R.; Nervi, C. Computational Study of the Electrochemical Reduction of W(CO)₄(2,2'-Dipyridylamine). *Inorg. Chim. Acta* **2018**, *470*, 373–378.
- (44) Ryan, D. E.; Cardin, D. J.; Hartl, F. η^3 -Allyl Carbonyl Complexes of Group 6 Metals: Structural Aspects, Isomerism, Dynamic Behaviour and Reactivity. *Coord. Chem. Rev.* **2017**, *335*, 103–149.
- (45) Tory, J.; Gobaille-Shaw, G.; Chippindale, A. M.; Hartl, F. Spectroelectrochemical Study of Complexes [Mo(CO)₂(η^3 -allyl)(α -Diimine)(NCS)] (α -Diimine = Bis(2,6-Dimethylphenyl)-Acenaphthenequinonediimine and 2,2'-Bipyridine) Exhibiting Different Molecular Structure and Redox Reactivity. *J. Organomet. Chem.* **2014**, *760*, 30–41.
- (46) Goodyear, J. W.; Hemingway, C. W.; Harrington, R. W.; Wiseman, M. R.; Brisdon, B. J. The Crystal Structure of [Mo(NCS)(CO)₂(η^3 -C₃H₅)(NCMe)₂]-MeCN and the Reactions of {Mo(CO)₂(η^3 -C₃H₅)⁺} Containing Species with Symmetric Alkynes. *J. Organomet. Chem.* **2002**, *664*, 176–181.
- (47) Agilent (2014). *CrysAlis PRO*. Agilent Technologies Ltd, Yarnton, Oxfordshire, England.
- (48) Palatinus, L.; Chapuis, G. *SUPERFLIP* – a Computer Program for the Solution of Crystal Structures by Charge Flipping in Arbitrary Dimensions. *J. Appl. Crystallogr.* **2007**, *40*, 786–790.
- (49) Betteridge, P. W.; Carruthers, J. R.; Cooper, R. I.; Prout, K.; Watkin, D. J.; IUCr. *CRYSTALS* Version 12: Software for Guided Crystal Structure Analysis. *J. Appl. Crystallogr.* **2003**, *36*, 1487–1487.
- (50) van der Sluis, P.; Spek, A. L. *BYPASS*: An Effective Method for the Refinement of Crystal Structures Containing Disordered Solvent Regions. *Acta Crystallogr. Sect. A* **1990**, *46*, 194–201.
- (51) Krejčík, M.; Daněk, M.; Hartl, F. Simple Construction of an Infrared Optically Transparent Thin-Layer Electrochemical Cell: Applications to the Redox Reactions of ferrocene, Mn₂(CO)₁₀ and Mn(CO)₃(3,5-di-*t*-Butyl-Catecholate). *J. Electroanal. Chem. Interfacial Electrochem.* **1991**, *317*, 179–187.
- (52) Mahabiersing, T.; Lyuten, H.; Nieuwendam, R. C.; Hartl, F. Synthesis, Spectroscopy and Spectroelectrochemistry of Chlorocarbonyl {1,2-Bis[(2,6-Diisopropylphenyl)imino]acenaphthene- κ^2 -N,N'}rhodium(I). *Collect. Czech. Chem. Commun.* **2003**, *68*, 1687–1709.
- (53) Parr, R. G.; Yang, W. *Density-Functional Theory of Atoms and Molecules*; Oxford University Press, 1989.
- (54) te Velde, G.; Bickelhaupt, F. M.; Baerends, E. J.; Fonseca Guerra, C.; van Gisbergen, S. J. A.; Snijders, J. G.; Ziegler, T. Chemistry with ADF. *J. Comput. Chem.* **2001**, *22*, 931–967.
- (55) Fonseca Guerra, C.; Snijders, J. G.; Te Velde, G.; Baerends, E. J. Towards an Order-N DFT Method. *Theor. Chem. Acc.* **1998**, *99*, 391–403.
- (56) Theoretical Chemistry, Vrije Universiteit, Amsterdam, T. N. ADF2013 SCM <http://www.scm.com> (accessed Jul 26, 2018).
- (57) Vosko, S. H.; Wilk, L.; Nusair, M. Accurate Spin-Dependent Electron Liquid Correlation Energies for Local Spin Density Calculations: A Critical Analysis. *Can. J. Phys.* **1980**, *58*, 1200–1211.
- (58) Becke, A. D. A New Inhomogeneity Parameter in Density-Functional Theory. *J. Chem. Phys.* **1998**, *109*, 2092.
- (59) Perdew, J. P. Density-Functional Approximation for the Correlation Energy of the Inhomogeneous Electron Gas. *Phys. Rev. B* **1986**, *33*, 8822–8824.
- (60) Perdew, J. P. Erratum: Density-Functional Approximation for the Correlation Energy of the Inhomogeneous Electron Gas. *Phys. Rev. B* **1986**, *34*, 7406–7406.
- (61) van Lenthe, E.; Ehlers, A.; Baerends, E.-J. Geometry Optimizations in the Zero Order Regular Approximation for Relativistic Effects. *J. Chem. Phys.* **1999**, *110*, 8943–8953.
- (62) Moussa, J.; Chamoreau, L.-M.; Degli Esposti, A.; Gullo, M. P.; Barbieri, A.; Amouri, H. Tuning Excited States of Bipyridyl Platinum(II) Chromophores with π -Bonded Catecholate Organometallic Ligands: Synthesis, Structures, TD-DFT Calculations, and Photophysical Properties. *Inorg. Chem.* **2014**, *53*, 6624–6633.
- (63) van Gisbergen, S. J. A.; Rosa, A.; Ricciardi, G.; Baerends, E. J. Time-Dependent Density Functional Calculations on the Electronic Absorption Spectrum of Free Base Porphin. *J. Chem. Phys.* **1999**, *111*, 2499–2506.
- (64) Rosa, A.; Baerends, E. J.; van Gisbergen, S. J. A.; van Lenthe, E.; Groeneveld, J. A.; Snijders, J. G. Electronic Spectra of M(CO)₆ (M = Cr, Mo, W) Revisited by a Relativistic TDDFT Approach. *J. Am. Chem. Soc.* **1999**, *121*, 10356–10365.
- (65) van Gisbergen, S. J. A.; Groeneveld, J. A.; Rosa, A.; Snijders, J. G.; Baerends, E. J. Excitation Energies for Transition Metal Compounds Applications to MnO₄⁻, Ni(CO)₄, and Mn₂(CO)₁₀. *J. Phys. Chem. A* **1999**, *103*, 6835–6844.
- (66) Wang, F.; Ziegler, T. A Simplified Relativistic Time-Dependent Density-Functional Theory Formalism for the Calculations of Excitation Energies Including Spin-Orbit Coupling Effect. *J. Chem. Phys.* **2005**, *123*, 154102.
- (67) Ziegler, T.; Rauk, A. Carbon Monoxide, Carbon Monosulfide, Molecular Nitrogen, Phosphorus Trifluoride, and Methyl Isocyanide as Sigma Donors and Pi Acceptors. A Theoretical Study by the Hartree-Fock-Slater Transition-State Method. *Inorg. Chem.* **1979**, *18*, 1755–1759.
- (68) Ziegler, T.; Rauk, A. On the Calculation of Bonding Energies by the Hartree Fock Slater Method. *Theor. Chim. Acta* **1977**, *46*, 1–10.
- (69) Chemcraft Program <http://www.chemcraftprog.com/index.html> (accessed Jul 26, 2018).
- (70) Graham, A. J.; Fenn, R. H. The Crystal Structure of Some Dicarboxyl-Allyl Derivatives of Substituted Carbonyls of Molybdenum (I). The Crystal Structure of (Isothiocyanato)dicarbonyl-2,2'-bipyridine- π -allylmolybdenum NCS(CO)₂(C₁₀H₈N₂)(π -C₃H₅)Mo. *J. Organomet. Chem.* **1969**, *17*, 405–422.
- (71) Liu, F. C.; Yang, P. S.; Chen, C. Y.; Lee, G. H.; Peng, S. M. Syntheses, Structures, and Dynamic Properties of M(CO)₂(η^3 -C₃H₅)(L-L)(NCBH₃) (M = Mo, W; L-L = Dppe, Bipy, En). *J. Organomet. Chem.* **2008**, *693*, 537–545.
- (72) Ascenso, J. R.; De Azevedo, C. G.; Calhorda, M. J.; De, M. A. A. F.; Costa, P.; Dias, A. R.; Drew, M. G. B.; Félix, V.; Galvão, A. M.; Romão, C. C. Synthesis, Bonding and Dynamic Behavior of *Fac*-[Mo(II)(CO)₂(η^3 -Allyl)] Derivatives. *J. Organomet. Chem.* **2001**, *632*, 197–208.
- (73) Faller, J. W.; Haitko, D. A.; Adams, R. D.; Chodosh, D. F. Aspects of Chirality Retention in Rearrangements of Pseudoctahedral

Molybdenum and Tungsten Complexes. *J. Am. Chem. Soc.* **1979**, *101*, 865–876.

- (74) Alonso, J. C.; Neves, P.; Da Silva, M. J. P.; Quintal, S.; Vaz, P. D.; Silva, C.; Valente, A. A.; Ferreira, P.; Calhorda, M. J.; Félix, V.; et al. Molybdenum η^3 -Allyl Dicarbonyl Complexes as a New Class of Precursors for Highly Reactive Epoxidation Catalysts with Tert-Butyl Hydroperoxide. *Organometallics* **2007**, *26*, 5548–5556.
- (75) Chabolla, S. A.; Dellamary, E. A.; Machan, C. W.; Tezcan, F. A.; Kubiak, C. P. Combined Steric and Electronic Effects of Positional Substitution on Dimethyl-Bipyridine Rhenium(I) Tricarbonyl Electrocatalysts for the Reduction of CO₂. *Inorganica Chim. Acta* **2014**, *422*, 109–113.
- (76) Vichova, J.; Hartl, F.; Vlcek, A. Wavelength-Dependent Photosubstitution and Excited-State Dynamics of [Cr(CO)₄(2,2'-Bipyridine)]: A Quantum Yield and Picosecond Absorption Study. *J. Am. Chem. Soc.* **1992**, *114*, 10903–10910.
- (77) Hartl, F.; Rosa, P.; Ricard, L.; Le Floch, P.; Zális, S. Electronic Transitions and Bonding Properties in a Series of Five-Coordinate “16-Electron” Complexes [Mn(CO)₃(L₂)]⁻ (L₂ = Chelating Redox-Active π -Donor Ligand). *Coord. Chem. Rev.* **2007**, *251*, 557–576.
- (78) van Outersterp, J. W. M.; Hartl, F.; Stufkens, D. J. Variable Temperature IR Spectroelectrochemical Investigation of the Stability of the Metal-Metal-Bonded Radical Anions [(CO)₅MnRe(CO)₃(L)]⁻ (L = 2,2'-Bipyridine (BPY), 2,2'-Bipyrimidine (BPYM), 2,3-Bis(2-Pyridyl)Pyrazine (DPP)) and [(CO)₅MnRe(CO)₃(L)Re(Br)(CO)₃]⁻ (L = BPYM, DPP) Controlled by the Lowest π^* (α -Diimine) Orbital Energy. *Organometallics* **1995**, *14*, 3303–3310.
- (79) An alternative structure of 6-coordinate [1-PrCN]⁻ has been suggested by DFT calculations on its possible triplet states. The paramagnetic equatorial form appears to be quite stable, revealing a changed η^2 -allyl coordination and a stronger Mo–PrCN bond. A detailed investigation of this interesting alternative was out of the scope of this work, but attention will be paid to it in the follow-up studies.
- (80) Stor, G. J.; Hartl, F.; van Outersterp, J. W. M.; Stufkens, D. J. Spectroelectrochemical (IR, UV/Vis) Determination of the Reduction Pathways for a Series of [Re(CO)₃(α -Diimine)L]^{0/+} (L' = Halide, Otf⁻, THF, MeCN, n-PrCN, PPh₃, P(OMe)₃) Complexes. *Organometallics* **1995**, *14*, 1115–1131.
- (81) Hartl, F.; Aarnts, M. P.; Nieuwenhuis, H. A.; Van Slageren, J. Electrochemistry of Different Types of Photoreactive Ruthenium(II) Dicarbonyl α -Diimine Complexes. *Coord. Chem. Rev.* **2002**, *230*, 107–125.
- (82) Zeng, Q.; Tory, J.; Hartl, F. Electrocatalytic Reduction of Carbon Dioxide with a Manganese (I) Tricarbonyl Complex Containing a Nonaromatic α -Diimine Ligand. *Organometallics* **2014**, *33*, 5002–5008

Table of Contents artwork

Substituents Control the Cathodic Path

